Chapter 5
Insights into Laser-Materials Interaction Through Modeling on Atomic and Macroscopic Scales

Maxim V. Shugaev, Miao He, Sergey A. Lizunov, Yoann Levy, Thibault J.-Y. Derrien, Vladimir P. Zhukov, Nadezhda M. Bulgakova and Leonid V. Zhigilei

Abstract Computer simulations and theoretical analysis of laser-materials interactions are playing an increasingly important role in the advancement of modern laser technologies and broadening the range of laser applications. In this chapter, we first provide an overview of the current understanding of the laser coupling and transient variation of optical properties in metals, semiconductors and dielectrics, with the focus on the practical implications on the energy deposition and distribution in the

M. V. Shugaev · M. He · L. V. Zhigilei (✉)
Department of Materials Science and Engineering, University of Virginia, 395 McCormick Road, Charlottesville, VA 22904-4745, USA
e-mail: lz2n@virginia.edu

M. V. Shugaev
e-mail: mvs9t@virginia.edu

M. He
e-mail: mh5wz@virginia.edu

S. A. Lizunov · Y. Levy · T. J.-Y. Derrien · V. P. Zhukov · N. M. Bulgakova
HiLASE Centre, Institute of Physics of the Czech Academy of Sciences, Za Radnicí 828, 25241 Dolní Břežany, Czech Republic
e-mail: lizunov@fzu.cz

Y. Levy
e-mail: levy@fzu.cz

T. J.-Y. Derrien
e-mail: derrien@fzu.cz

V. P. Zhukov
e-mail: zukov@ict.nsc.ru

N. M. Bulgakova
e-mail: bulgakova@fzu.cz

S. A. Lizunov
Institute of Thermophysics SB RAS, 1 Lavrentyev Ave, 630090 Novosibirsk, Russia

V. P. Zhukov
Institute of Computational Technologies SB RAS, 6 Lavrentyev Ave, 630090 Novosibirsk, Russia

© Springer Nature Switzerland AG 2018

P. M. Ossi (ed.), *Advances in the Application of Lasers in Materials Science*,
Springer Series in Materials Science 274,
https://doi.org/10.1007/978-3-319-96845-2_5

irradiated targets. The continuum-level modeling of the dynamic evolution of laser-induced stresses, nonequilibrium phase transformations, and material redistribution within the laser spot are then discussed, and the need for the physical insights into the mechanisms and kinetics of highly nonequilibrium processes triggered by the laser excitation is highlighted. The physical insights can be provided by atomistic modeling, and several examples are discussed where large-scale molecular dynamics simulations are used for investigation of the mechanisms of the generation of crystal defects (vacancies, interstitials, dislocations, and twin boundaries) and the material redistribution responsible for the formation of laser-induced periodic surface structures in the single-pulse ablative regime. The need for the integrated computational approach fully accounting for the strong coupling between processes occurring at different time- and length-scales is highlighted.

5.1 Introduction

The continuous progress in the advancement of laser applications is increasingly relying on thorough theoretical understanding of laser-induced processes that control the structural and phase transformations responsible for material modification, selective removal and/or transfer. Experimental diagnostics capable of resolving the laser-induced processes on femto-/picosecond time-scales and simultaneously on sub-micrometer length-scales, however, are currently limited to specific systems and irradiation conditions [1–3]. Even with the advancement of existing and the development of new time-resolved diagnostic methods, the experimental probing alone is unlikely to completely uncover the relationships between numerous processes involved in laser-matter interactions, which take place simultaneously or sequentially with overlap in time and space. Hence, numerical simulation of processes occurring in laser-irradiated materials is an invaluable tool for understanding the complex phenomena of laser-materials interactions, especially when materials are driven far out of electronic, thermal, and mechanical equilibrium [4]. A combination of numerical simulation and experimental probing of laser-induced processes performed for the same experimental conditions is likely to be the most efficient way of gaining deep insights into the rapid structural and phase transformations triggered by the laser excitation.

In this chapter, we provide an overview of theoretical treatment and numerical modeling of different stages of laser-materials interactions, from the laser excitation of the electronic sub-system in the material to the thermal and mechanical response to the laser energy deposition leading to material modification, redistribution, or ejection from the irradiated target. The overview is focused on computational predictions that can be directly mapped to experimental observations and used for optimization of laser processing conditions in practical applications. We start with analysis of the transient modification of optical properties due to the laser-induced electronic excitation, as it defines the fraction of the incident laser energy that is absorbed by the irradiated material and its initial distribution in the target. The solid knowledge

of the laser energy deposition and redistribution enables a reliable analysis of the material response to the rapid laser heating, which may involve plastic deformation, melting and resolidification, hydrodynamic flow of molten material, photomechanical damage/spallation, explosive boiling of material superheated up to the limit of its thermodynamic stability, and the ejection of material from the target driven by the relaxation of laser-induced stresses, the explosive release of vapor, and/or material ionization and charge separation. Many of the processes involved in laser-materials interactions have been addressed in atomistic or continuum-level simulations, and have been reviewed in chapters published as follow ups on two earlier editions of the School on Lasers in Materials Science [5–8]. In this chapter, we focus our attention on methods capable of addressing the processes occurring on the scale of the whole laser spot as well as on multiscale computational approaches where atomistic simulations inform the larger-scale continuum models on the kinetics and mechanisms of laser-induced structural and phase transformations, and help to design advanced continuum-level models fully accounting for the complexity of short pulse laser-materials interactions.

The variation of optical properties of metals, semiconductors and dielectrics excited by the laser irradiation are discussed next in Sect. 5.2, the continuum-level modeling of thermal and mechanical processes occurring on the scale of the laser spot is reviewed in Sect. 5.3, and several examples of the use of atomistic molecular dynamics method for revealing the processes responsible for material modification by short laser pulses are provided in Sect. 5.4. Finally, in Sect. 5.5, we briefly outline the prospects for the advancement of the computational treatment of the complex phenomena of laser-materials interactions.

5.2 Transient Response of Materials to Ultrafast Laser Excitation: Optical Properties

In this section, we provide a brief overview of several analytical models developed to describe the *optical* response of laser-irradiated materials, which is swiftly changing already during the laser pulse action and continue to evolve after pulse termination. We focus on simplified analytical models, which can be integrated into large-scale continuum or atomistic simulations of ultrashort laser-matter interaction. While for the bandgap materials the existing optical models usually account for the dynamic variation of surface reflectivity due to generation of charge carriers in the conduction band, in the case of metals the majority of simulations reported in literature are based on an assumption of constant reflectivity equal to that of a cold metal at a specific wavelength. This can lead to misinterpretation of experimental data, as the optical properties (both reflectivity and absorption coefficient) of the free electron population in metals may change considerably when the energy density of up to several eV per electron is deposited by the laser pulse. When the surface reflectivity strongly varies upon ultrafast laser excitation of a sample, the actual absorbed energy can be,

depending on the electronic structure of the material, either under- or overestimated. While many details of the transient optical response of materials undergoing strong electronic excitation and rapid equilibration are still not fully understood, the simplified models discussed in this section may provide general guidance for interpretation of experimental observations.

5.2.1 Metals: Transient Optical Properties

Theoretical description of the optical response of metals as well as bandgap materials upon their ionization with generation of a dense free-electron plasma is usually based on the theory proposed by Paul Karl Ludwig Drude in 1900 [9]. The Drude theory was developed for explaining the electrical conduction in metals under the classical assumption that free electrons can be represented as particles scattered in collisions with immobile ions. It was refined by Hendrik Antoon Lorentz who proposed that the mean free path of electrons was limited by collisions. This simple theory gives a physical justification for Ohm's law and can predict the electron current in metals under the action of electromagnetic waves. As the frequency-dependent dielectric function of a material is directly related to the oscillating current of free electrons, the Drude theory is widely used for describing the free-carrier contribution to the optical response of solids to laser light (known as the Drude model or sometimes the Drude-Lorentz model) [10, 11].

5.2.1.1 The Drude Model

The Drude model (or free electron model) provides the basic formulation of the free carrier contribution in the material response to electromagnetic waves of a specific angular frequency ω via the expression for the complex dielectric function, which reads in the general form as [11, 12]:

$$\varepsilon = \varepsilon_{\text{core}} + i\frac{n_e e^2 \tau_c}{\omega \varepsilon_0 m_e^*(1 - i\omega\tau_c)}. \tag{5.1}$$

Equation (5.1) can be rewritten as

$$\varepsilon = \varepsilon_1 + i\varepsilon_2 \text{ with}$$
$$\varepsilon_1 = \varepsilon_{\text{core}} - \frac{n_e e^2 \tau_c^2}{\varepsilon_0 m_e^*(1 + \omega^2\tau_c^2)} \text{ and } \varepsilon_2 = \frac{n_e e^2 \tau_c}{\omega \varepsilon_0 m_e^*(1 + \omega^2\tau_c^2)}. \tag{5.2}$$

Here n_e and e are the free electron density and elementary charge, $1/\tau_c$ is the collision frequency of electrons. The collisions between electrons and between electrons and lattice atoms/ions provide damping of the optical response of material to laser radiation. When free electrons are moving in a periodic potential of the lattice in a

solid medium, they respond to external forces differently than in vacuum. To simplify the description of this effect, the effective mass m_e^* is introduced, which is usually considered to be constant independent of the excitation conditions. $\varepsilon_{\text{core}}$ is a core dielectric function, which is introduced to approximate the interband contributions (absorption of electromagnetic radiation by an electron in an occupied state below the Fermi level with transition to an unoccupied state in a higher band) [11]. This part of the dielectric function is usually considered as independent of frequency. In vacuum $\varepsilon_{\text{core}} = 1$ and often the same is considered for metals [10, 11]. Note that, according to the Drude model, the dielectric permittivity is connected with the electric conductivity $\sigma(\omega)$ in metals as $\varepsilon = 1 + i\sigma(\omega)/\varepsilon_0\omega$.

It is seen from (5.2) that ε_1 becomes negative starting from some frequency $\omega_p = \sqrt{n_e e^2/\varepsilon_0 \varepsilon_{\text{core}} m_e^*}$, taking into account that $(1/\tau_c) \ll \omega_p$. At this characteristic frequency ω_p, called plasma frequency, the response of the material changes from a metallic to a dielectric one. The electromagnetic field with angular frequency below the plasma frequency cannot penetrate the material. This corresponds to the collisionless plasma regime, when the light is totally reflected. In metals, electromagnetic waves can penetrate a very thin surface layer whose size is determined by the electron collision frequency $(1/\tau_c)$ and can be calculated from the dielectric function, see below.

The optical properties of cold metals are reasonably well described by the Drude model in infrared and, partially, visible spectral ranges via adjusting the plasma and collision frequencies, while at higher frequencies the model fails [10]. The reasons for the failure include an increasing contribution of intraband transitions and an enhanced sensitivity of the electromagnetic wave to surface roughness at shorter laser wavelengths. To extend the description for a wider spectral range, several modifications of the Drude model have been proposed.

5.2.1.2 The Combined Drude-Lorentz Model

The Lorentz model was developed for insulating materials, assuming that the electrons are bound to the nuclei in a similar way as small light balls can be bound to large heavy balls by springs [13]. Under the action of an external periodically-varied force (electromagnetic wave), such system has resonant frequencies (harmonic oscillators). Then, the complex dielectric function of a material can be described by accounting for both free and core (bound) electrons through a combination of the Drude and Lorentz models [14, 15]:

$$\varepsilon = \varepsilon_D + \varepsilon_L, \tag{5.3}$$

where ε_D is given by (5.1), and ε_L is the Lorentzian term written in the general form as [13, 14, 16]

$$\varepsilon_L = -\sum_{l=1}^{N} \frac{f_l \Omega_{L,l}^2}{(\omega^2 - \Omega_{L,l}^2) - i\omega\Gamma_{L,l}}. \tag{5.4}$$

Here $\Omega_{L,l}$ is a resonant frequency l ($l = 1, \ldots, N$) with a weighting factor f_l defining the fraction of electrons that are bound to this frequency ($\sum_{l=1}^{N} f_l = 1$), and $\Gamma_{L,l}$ is the damping constant. Adding one or several Lorentzian terms to the Drude model enables expansion of the accessible spectral range toward shorter wavelengths, where the optical properties can be satisfactorily described at a fixed temperature via fitting the model parameters ($\varepsilon_{\text{core}}$, ω_p, τ_c, $\Omega_{L,l}$, $\Gamma_{L,l}$, f_l) [14, 16–18].

It is clear that the above approach gives a rather schematic description of different contributions and parameters affecting the optical response of metals, and its application to simulations of laser-matter interactions must involve a fitting procedure. However, the Drude model and the combined Drude-Lorentz model represent a valuable tool that enables an effective description of the swift changes in the optical properties of solids irradiated by ultrashort powerful laser pulses within the framework of large-scale continuum or atomistic models.

5.2.1.3 High Free-Electron Temperatures: Plasma-like Behavior

When the electron temperature in metals (T_e) approaches the Fermi temperature (T_F), the electron gas starts to behave as a hot dense plasma with associated change in optical response ([19] and references therein) that has to also be accounted for in simulations. The dielectric permittivity at the limit of the hot electron plasma ($T_e \gg T_F$), ε_p, with the Maxwellian distribution function can be expressed in the following form [19–22]:

$$\varepsilon_p = 1 + i\frac{4\omega_p^2}{3\omega(k_B T_e)^{5/2}\sqrt{\pi}} \int_0^\infty \mathrm{d}E_e \frac{E_e^{3/2}\exp(-E_e/k_B T_e)}{-i\omega + 3\sqrt{\pi/2}(k_B T_e/E_e)^{3/2}\nu_{ei}^T G}, \tag{5.5}$$

where E_e and T_e are the electron energy and temperature, respectively; k_B is the Boltzmann constant; $\nu_{ei}^T = 4\sqrt{2\pi}Zn_i e^4 \ln\Lambda / \left(\sqrt{m_e}k_B^{3/2}T_e^{3/2}\right)$ is the electron-ion collision frequency with the Coulomb logarithm, $\ln\Lambda$, which can be approximately taken to be equal to 2 at the electron temperatures of the order of 10 eV [23]; the factor $G = \left(\nu_{ei}^T/\gamma_\sigma + (1-2i)\omega\right)/\left(\nu_{ei}^T + (1-2i)\omega\right)$ with $\gamma_\sigma \approx (0.87 + Z)/(2.2 + Z)$ accounts for the electron-electron collisions [22]; Z is the number of free electrons per ion in the metal, and $n_i = n_e/Z$ is the number density of ions. Note that generally Z can vary upon irradiation of transition metals by ultrashort laser pulses due to excitation of d-electrons [24].

By convention, the description of the optical properties of metals can be divided into three regimes depending on the electron temperature: (1) low electron temperatures, much smaller than T_F; (2) large electron temperatures, above T_F, and (3) intermediate electron temperatures, when both metallic and plasma behavior of the

conduction electrons can be manifested. In the examples shown in Fig. 5.1, the following matching between the metallic and plasma ranges of the dielectric function was used:

$$\varepsilon = \begin{cases} \varepsilon_m, & T_e < 0.3T_F \\ \varepsilon_m + \varepsilon_p, & 0.3T_F < T_e < T_F \\ \varepsilon_p, & T_e > T_F \end{cases} \tag{5.6}$$

Here ε_m is calculated according to (5.1) or (5.3). Note that different methods were proposed for bridging the metallic and nondegenerate plasma behaviors via power [19] or linear [25] functions. However, we did not find much difference in the simulation results after applying the different functions. Expression (5.6) gives a sufficiently smooth transition between the two types of metal optical response.

5.2.1.4 Reflection and Absorption Coefficients

As soon as the dielectric function is determined by one of the methods described above, the reflection and absorption coefficients of a material exposed to a short pulse laser heating can be calculated using the Fresnel equations. The refractive index n and the extinction coefficient k are expressed as

$$n = \sqrt{\frac{1}{2}\left(\varepsilon_1 + \sqrt{\varepsilon_1^2 + \varepsilon_2^2}\right)}, \tag{5.7}$$

$$k = \sqrt{\frac{1}{2}\left(-\varepsilon_1 + \sqrt{\varepsilon_1^2 + \varepsilon_2^2}\right)}. \tag{5.8}$$

Then the absorption α and reflection R coefficients are calculated as follows:

$$\alpha = \frac{4\pi k}{\lambda}, \tag{5.9}$$

$$R = \frac{(n-1)^2 + k^2}{(n+1)^2 + k^2}. \tag{5.10}$$

Here λ is the laser wavelength and the expression for R is given for the normal incidence of the laser beam. The absorption length $l_{ab} = 1/\alpha$ characterizes the depth of electromagnetic wave penetration into metallic sample. For an arbitrary angle of incidence, the Fresnel relation for R includes the angular dependence, which is a function of the light polarization direction relative to the beam incidence [26]. Additionally, when the surface layer of an irradiated material is strongly inhomogeneous (either in terms of composition or due to strong gradients of the electron and/or lattice temperatures and the electron density), application of the multilayer

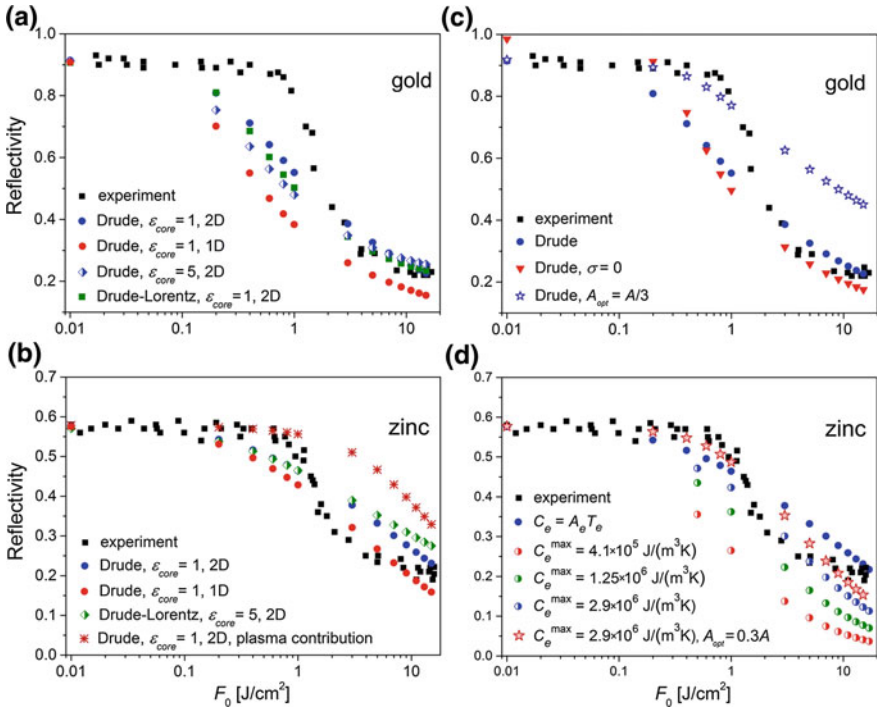

Fig. 5.1 Comparison of the reflectivity of gold and zinc as a function of the average fluence, F_0, obtained in TTM modeling combined with different models of the optical response. The target is irradiated by 66-fs Gaussian laser pulses at 800 nm wavelength. The experimental data were obtained using the hemiellipsoidal metallic reflector technique [34, 36]. Results obtained with the Drude model, (5.1), and the combined Drude-Lorentz model, (5.3), are marked as "Drude" and "Drude-Lorenz" respectively. The simulated reflectivity with integration over the irradiation spot is marked as 2D. 1D corresponds to the simulated reflectivity at the center of the irradiation spot, where $F = 2F_0$. To match the experimental data [36] at low fluences, surface roughness σ was set to 36 and 17 nm for zinc and gold, respectively, unless otherwise is specified. **a** Results for gold. The plasma response model was included in the simulations, but it does not give a noticeable effect in the studied fluence range and is therefore not shown here. **b** Results for zinc without and with plasma contribution, (5.6). **c** The Drude model with $\varepsilon_{\text{core}} = 1$ for gold: comparison of 2D simulations with and without accounting for surface roughness and under assumption that only ~30% of free electrons contribute to the optical response. **d** Simulations for zinc (2D-TTM with the Drude model at $\varepsilon_{core} = 1$) with the heat capacity calculated as the linear dependence $C_e = A_e T_e$ over the whole fluence range and with saturation at the values given in the legend. The data obtained under assumption that only ~30% of free electrons contribute to the optical response are shown by star symbols

approach for reflectivity calculations can be useful for achieving a better agreement with experimental data [12, 27, 28].

5.2.1.5 Surface Roughness Effect on Reflectance

The optical properties of material surfaces are dependent on their quality (primarily the surface roughness, oxidation, contamination, etc.) [29]. The handbooks of optical properties provide the data for thoroughly polished metals up to a mirror quality [30]. In many experiments on laser-matter interaction, the reflection coefficients of virgin surfaces can differ (usually are smaller) compared to the handbook data. For rough surfaces with the reflectivity close to the mirror quality ($\sigma \ll \lambda$, where σ stands for the mean-square roughness size), the following expressions can be used to account for the surface roughness in specular and diffuse reflectances, $R_{s,\text{rough}}$ and $R_{d,\text{rough}}$ respectively [31, 32]:

$$R_{s,\text{rough}} = R\exp\left(-\left(\frac{4\pi\sigma}{\lambda}\right)^2\right), \quad R_{d,\text{rough}} = R\left(\frac{4\pi\sigma}{\lambda}\right)^2 \tag{5.11}$$

where R is the reflection coefficient for the ideally polished surface.

5.2.1.6 Two-Dimensional Two-Temperature Modeling (2D-TTM) of Metal Reflectivity Under Conditions of Ultrafast Laser Irradiation

The measurements of the dynamic reflectivity of material samples irradiated with ultrashort laser pulses are usually based on the two major techniques: pump-probe temporally-resolved reflectivity studies [33] and integral measurements of the reflected light using, for example, a hemiellipsoidal metallic reflector technique [34]. Both techniques assume that the light is reflected from a non-uniformly heated laser-irradiation spot that implies a necessity of 2D modeling. Even for the pump-probe technique, the probe pulse focused on a central area of the Gaussian irradiation spot can exhibit averaging over the non-uniformly excited area of the spot. Here, to evaluate the validity of different optical response models, we present the results of simulations based on the two-temperature model (TTM). The TTM is based on the assumption that, during the laser pulse, the laser energy is absorbed by the conduction electrons, which are heated to a high temperature, while the lattice remains cold. As a result, the heat transfer in such nonequilibrium system can be described by two heat flow equations, for electrons and lattice, with the heat exchange between them [35]. We use a "quasi-2D" approach, at which the heat flow simulations were performed only in the direction toward the sample depth, while the reflectivity was integrated over the irradiated spot. Such approach is justified by a small laser-affected depth compared to a typical laser spot size. An implicit numerical scheme was used to solve the TTM equations with integration using the Thomas algorithm. The time and spatial steps were thoroughly checked with respect to the numerical scheme convergence for both the temperature evolution and the integral reflectivity.

Figure 5.1 presents the results of numerical simulations for gold and zinc samples irradiated by single femtosecond laser pulses (66 fs FWHM) of Ti:sapphire laser (800 nm wavelength) with direct comparison to the reflectivity measurements using the hemiellipsoidal metallic reflector technique [36] . The simulations were based on the TTM, similar to that described in [37] but extended to two dimensions to simulate the integral reflected light. All of the optical models discussed above were used in an attempt to find the best agreement between the modeling and experiments.

The laser pulse was assumed to be temporally and spatially Gaussian. Since no results of ab initio calculations of thermophysical parameters of the electronic subsystem based on the electron density of states (DOS) [24, 38] are available for zinc, a simplified dependence of the heat capacity $C_e = A_e T_e$ and a constant electron-lattice coupling factor g [36, 39] were used in the calculations for Zn. The electron thermal conductivity was taken similarly to [24] as $K_e(T_e, T_l) = v_F^2 C_e(T_e)\tau_c(T_e, T_l)/3$, where v_F is the Fermi velocity. The collision frequency of free electrons was approximated via the sum of electron-electron and electron-phonon scattering rates as $1/\tau_c = 1/\tau_{e-e} + 1/\tau_{e-ph} = AT_e^2 + BT_l$ [24]. The coefficients A and B were assumed to be constant and were estimated as described in [40], which yielded $A = 1.805 \times 10^6$ K^{-2} s^{-1} and $B = 1.82 \times 10^{12}$ K^{-1} s^{-1} with the plasma frequency $\omega_p = 2.05 \times 10^{16}$ s^{-1}.

In the most simulations, the same τ_c values were used in the thermal conductivity expression and in the Drude model, (5.1) . It was found that the estimated B value did not give a reasonable agreement with the measured optical properties of well-polished zinc samples [16]. To fit the room temperature reflectivity, the scaling factor $k_s = 3$ was introduced similarly to [19], which yielded the final $B = 5.46 \times 10^{12}$ K^{-1} s^{-1}. As noted in [41, 42], not all electron-electron collisions can contribute to the material optical response. To account for this effect, in a number of simulations the A value was changed in the dielectric function to $A_{\text{opt}} = \eta A$ with introducing a scaling factor $\eta < 1$.

For the simulations with the combined Drude-Lorentz model, the single Lorentzian term was used with parameters that correspond to Fit #1 from [16]. In order to reduce the surface reflectivity reported in literature for highly polished zinc samples [16] to the experimental values of work [36] at low fluences, the surface roughness parameter $\sigma = 36$ nm was chosen, assuming the specular reflection, i.e., the first expression in (5.11).

The same 2D-TTM simulations were performed for gold with parametrization from [43]. The n and k values were taken from [30]. To fit the experimental reflectivity at low fluences reported in [36], the mean-square surface roughness of 17 nm was introduced. In the case of the combined Drude-Lorentz model, five Lorentzian terms were taken into account for gold with the parameters from [17]. The simulations were performed in the wide range of the laser fluence from 0.01 up to 20 J/cm^2 (average fluence over the irradiation spot).

Figure 5.1a, b show the results of the application of models described above to gold and zinc, respectively, and the results are compared with experimental measurements performed with the hemiellipsoidal metallic reflector technique [36] (black squares). For gold, Fig. 5.1a, the simulation data are presented for the Drude model, (5.1)

with two values of $\varepsilon_{\text{core}} = 1$ (blue dots) and 5 (blue half-filled diamonds), and the combined Drude-Lorentz model, (5.3) with $\varepsilon_{\text{core}} = 1$ (green squares). As can be seen, all models give essentially the same results and are not in a good agreement with the experimental data in the fluence range of ~0.2–1.5 J/cm^2, while at higher and lower fluences the simulation results are satisfactory. It should be noted that variation of $\varepsilon_{\text{core}}$ makes it possible to shift the reflectivity to a higher level at large laser fluences. In a number of studies it is argued that not all free electrons contribute to the optical response of metals and, hence, the effective electron-electron collision frequency in the dielectric function must be reduced compared to that responsible for the electron thermal conductivity [41, 42]. The simulations for gold have shown that, when accounting for this effect, it is possible to achieve a better agreement with the experimental data at laser fluences up to ~1 J/cm^2, while at higher fluences a considerable deviation between the experimental and theoretical data arises (blue-edged stars in Fig. 5.1c, $A_{\text{opt}} = A/3$).

The plasma response model was included to the simulations for gold, but it does not give a noticeable effect in the studied fluence range (therefore not shown in Fig. 5.1). It should be noted that the temperature maximum achieved in simulations was only slightly higher than the Fermi temperature of gold, which explains the small plasma contribution. For zinc, where the maximum temperature at the highest simulated fluence was around $2T_F$, the plasma effect on reflectivity is substantial, as shown in Fig. 5.1b (asterisks). The addition of the hot-plasma behavior to the optical response makes it possible to keep the reflectivity at a constant level up to $F_0 \approx 1$ J/cm^2, as observed experimentally. However, at higher fluences the plasma-like optical model yields a much slower decrease of the reflectivity as compared to the experimental measurements. Red dots in Fig. 5.1a, b show the results of 1D simulations for gold and zinc, respectively, performed at laser fluences that correspond to the center of the laser spot. The results demonstrate that 1D modeling can considerably overestimate the total absorbed laser energy, as clearly exemplified by the results shown for gold.

The simulation data obtained for gold with the Drude model and $\sigma = 0$ (ideally smooth surface, red triangles in Fig. 5.1c) overestimate the reflectivity at low fluences and underestimates at high fluences. As seen from Fig. 5.1b, the simulation results for zinc are not satisfactory almost in the whole range of laser fluences. The possible reasons of the discrepancy between the computational predictions and experimental data are discussed below.

5.2.1.7 Importance of the Thermophysical Properties of the "Free Electron Gas" for Description of Optical Response of Metals

As mentioned above, for the free electron population in zinc we used the simple linear dependence of the heat capacity on the electron temperature, $C_e = A_e T_e$ [37, 39], in view of absence of other data. At high free-electron temperatures, close to or above T_F, the heat capacity is expected to saturate at a value of the order of that of non-degenerate gas, $1.5 k_B n_e$, though plasma non-ideality at high densities as well as incomplete equilibrium [44] can influence this saturation value. According to DOS

simulations [24, 38], the majority of metals exhibit a tendency of the heat capacity saturation at high electron temperatures (note that the temperature of free electrons is considered here as a measure of their average energy even when the electrons are not fully thermalized immediately after ultrashort laser excitation). Figure 5.1d presents the 2D-TTM simulation data for zinc with the Drude model used to account for the optical response. Blue dots are predicted by assuming the linear electron temperature dependence of the heat capacity ($C_e = A_e T_e$ with $A_e = 81.9$ J/(m^{3}K)) in the whole range of laser fluences. The other half-filled dots show the results of calculations where the linear dependence was used up to a certain electron temperature, above which the value of C_e was fixed (kept constant upon further heating of the electrons). The results are shown for the following three levels of saturation of C_e: $C_e^{\max} = 4.1 \times 10^5$ J/(m^{3}K), 1.25×10^6 J/(m^{3}K), and 2.9×10^6 J/(m^{3}K). We note that $C_e^{\max} = 2.9 \times 10^6$ J/(m^{3}K), which corresponds to $T_e \approx 35{,}000$ K, is close to the values of the electron heat capacity of a number of metals at temperatures where the saturation becomes pronounced [24], and this value gives the best fit to the experimental data for zinc at fluences >1 J/cm^2. Accounting for the limited contribution of the electron-electron collision frequency in the dielectric function leads to even better agreement between simulations and experiment (red-edged stars in Fig. 5.1d, $A_{\text{opt}} = A/3$). To further improve the simulation accuracy at higher fluences, $\varepsilon_{\text{core}} > 1$ can be introduced to account for interband transitions. However, the fluence range where the reflectivity exhibits a sudden drop for both metals is not still properly described that calls for further studies.

The following reasons can be hypothesized to be responsible for the observed sudden drop of the reflectivity and the discrepancy between the experimental and modeling data:

(i) At the first turn, it can be the effect of unsatisfactory description of thermophysical properties of the electron subsystem of the material (note that the electron thermal conductivity of free electrons is also affected by the temperature dependence of the electron heat capacity, see above). As demonstrated in Fig. 5.1d, the choice of the temperature dependence of the heat capacity has a strong effect on the calculated reflectivity. The electron-lattice coupling factor g, which is considered here to be constant for zinc, can also have an impact on the transient optical response of metals, and its temperature dependence [24] should be accounted for in interpretation of the results of pump-probe experiments. However, during irradiation by femtosecond laser pulses, when the electron-lattice coupling is insignificant, the influence of g on the incident pulse reflection should not be pronounced.

(ii) We assume here that the surface roughness behaves in the same manner irrespectively to the electron temperature. However, at high laser fluences, the incident laser wave can be scattered differently than at low fluences. As a result, the light absorption can be significantly altered by the interference between the scattered surface wave and the incident laser wave. For instance, for linearly polarized laser light, the interference effect results in the transient periodic absorption pattern leading to the formation of laser-induced periodic surface

structures (LIPSS) at relatively low fluences, near the melting threshold [45, 46], as well as in the regimes of the developed ablation [47] . However, in the ablative regimes the LIPSS can exhibit very high regularity [47], indicating a change in laser-surface coupling.

(iii) The collision frequency of the electrons does not satisfy the simple relation $1/\tau_c = AT_e^2 + BT_l$ at high heating rates/values, and the A and B coefficients can be variable, thus affecting the temperature dependence of the electron thermal conductivity (see above). Additionally, the fraction of free electrons actively participating in the material optical response can also be changing with the electron temperature, thus leading to the variation of A_{opt} [42].

(iv) For the adequate comparison of simulation results with experimental data, the multilayer model must be used for metals at high heating rates to account for a highly inhomogeneous temperature profile that can be formed even within the absorption depth.

(v) The effects of nonequilibrium within the electron subsystem at high-power laser heating are still poorly understood but can have important consequences on the reflectivity of metals.

The simple optical models considered above are needed for large-scale multiphysics simulations of laser interactions with metals, where ab initio models cannot be applied. However, it must be noted that even the existing ab initio models, which require large computational resources, cannot provide an adequate description of the experimental data [48]. Two examples of computational analysis of ultrashort laser interaction with metals, where the dynamic optical response plays a key role, are presented below.

5.2.1.8 Dynamic Optical Response of Metals to Ultrashort Laser Pulses

Surface plasmon-polariton decay length. The origin of LIPSS produced on material surfaces by ultrashort laser pulse irradiation is mainly attributed to the interference of the incident and surface scattered electromagnetic waves [45]. However, the factors affecting the quality of the surface pattern are still debated. Recently, two opposite views on the problem of periodic laser-induced pattern quality were published. Öktem et al. [49] state that, for inscription of a highly regular structure on a metallic surface, the distant points of the irradiation spot must interact via a mutual electric field. Hence, the surface scattered wave has to propagate a distance covering the whole irradiation spot. Limiting the laser-irradiation spot diameter to several wavelengths (12 μm in [49]) can facilitate a better interaction between the surface electromagnetic waves excited in different parts of the irradiation spot, thus enabling better quality of LIPSS. On the contrary, Gnilitskyi et al. [47] have demonstrated experimentally and computationally that metals with a short decay length of the scattered waves enable imprinting of highly regular LIPSS on their surfaces. Although a small irradiation spot size was used in [47] (10.4 μm), it was proven that limiting the interaction between the scattered surface waves (surface plasmon polaritons, or SPP as

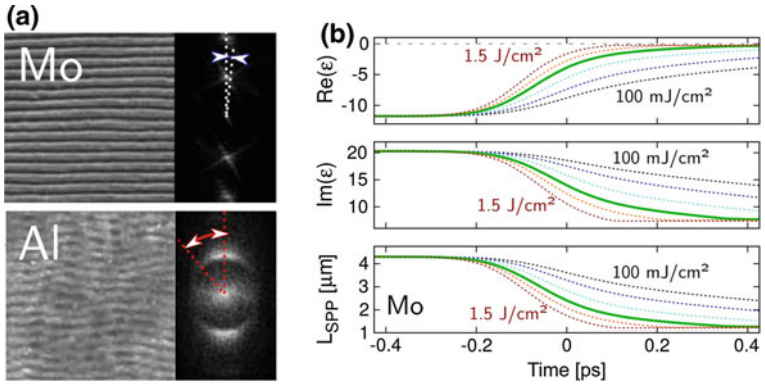

Fig. 5.2 **a** LIPSS imprinted by ultrashort (213 fs) laser pulses at the wavelength of 1030 nm on surfaces of molybdenum (top) with $L_{SPP} \approx 4.3$ μm and aluminum (bottom) with $L_{SPP} \approx 65$ μm under similar irradiation conditions. On the right, 2D Fourier transforms of the images are presented, demonstrating the dispersion of the LIPSS orientation angle (5.3° for Mo and 26.7° for Al). **b** The temporal evolution of the real and imaginary parts of the dielectric function and the SPP decay length, L_{SPP}, for molybdenum under the conditions of (**a**), predicted in TTM simulations supplemented by the Drude model. Colored lines correspond to decreasing fluence from left to right: 1.5, 1, 0.69, 0.4, 0.2, and 0.1 J/cm^2. The results are adapted from [47]

a particular case) allows preserving their coherence with the incident laser light and creation of a regular periodic pattern of light absorption, free of bifurcation points. Figure 5.2a shows LIPSS imprinted on two metals, Mo with the decay length of SPP $L_{SPP} \approx 4.3$ μm (top) and Al with $L_{SPP} \approx 65$ μm (bottom), that clearly demonstrates this concept. On the right from LIPSS images, the estimated dispersion of the LIPSS orientation angle is presented, showing only 5.3° for Mo and 26.7° for Al. This finding is supported by the work of Ruiz de la Cruz et al. [50], where the highly regular periodic surface structures were formed on Cr surfaces with the irradiation spot diameter of 80 μm, much larger than L_{SPP} (4.1 μm [47]). Note that all LIPSS discussed above were produced at near-IR laser wavelength. The plasmon polariton theory proposed in [47] predicts the tendency of L_{SPP} decreasing with wavelength so that the highly regular LIPSS can be imprinted on surfaces of a wider number of metals at visible and near UV spectral range of laser radiation.

The above-cited L_{SPP} values were estimated based on the metal properties under normal conditions. An important question arises on how the SPP decay length evolves upon excitation of metal surfaces by an ultrashort laser pulse. This question was addressed in a series of TTM simulations supplemented by the Drude model, (5.1), (5.7)–(5.10), to account for the transient variation of the optical properties. The simulations have revealed that L_{SPP} decreases upon excitation by ultrashort laser pulses [47] (Fig. 5.2b, the case of molybdenum), thus enhancing the feasibility of obtaining highly regular periodic structures. An important conclusion was made that the tendency of decreasing L_{SPP} upon ultrashort laser irradiation is inherent to all metals. Furthermore, the transient L_{SPP} value is smaller for higher laser fluences,

Fig. 5.2b, thus supporting the mechanism of the efficient LIPSS formation in the ablation regimes.

Evolution of modulated absorption pattern under the conditions of LIPSS formation. Another TTM simulation example, where modeling of the optical response has proven to be of high importance for understanding of the physical processes, is related to the temporal evolution of the modulated temperature profile generated by the interference of the incident and surface scattered electromagnetic waves upon ultrashort laser irradiation [40, 51]. As mentioned above, the formation of periodic surface patterns is believed to be triggered by the periodic absorption of the linearly polarized laser light [45]. The questions on how strong can be the modulation of the lattice temperature produced by the wave interference and how long the temperature modulation can survive on material surface are of high importance for understanding of the post-irradiation evolution of material toward the periodic surface relief. These questions were addressed in [40, 51], where the results of 2D-TTM simulations performed for different materials (titanium, gold, silicon, fused silica) under the assumption that the incident laser intensity is spatially modulated across the beam diameter, as shown in Fig. 5.3a, are reported. It was demonstrated that once free electrons absorbing the laser light experience a spatial modulation of their temperature with the periodicity close to the laser wavelength, they transfer this modulation to the lattice. The periodic lattice temperature profile can survive on the surface up to hundreds of picoseconds even in metals, where high heat conduction effectively smooths the heating inhomogeneity.

Figure 5.3b underlines the importance of taking into account the dynamical change of the optical properties of irradiated materials on the example of gold (800 nm wavelength, 100 fs pulse duration, laser fluence of 1.1 J/cm^2) [51]. It shows the temporal evolution of the surface temperature modulation determined by the parameter $a_l = T_{l,\max} - T_{l,\min}$ (the difference between the maximum and minimum of the lattice temperature in the periodic modulation) called the modulation amplitude. The simulations performed with constant reflection and absorption coefficients taken at their room temperature values (dashed line) yielded only slight modulation of the order of 40 K. The a_l value is first increasing due to lattice heating during the electron-lattice thermalization stage (approximately 10 ps) and then starts to gradually decrease as the result of smoothing the inhomogeneous temperature distribution by heat conductivity. When the dynamic change of the optical properties has been implemented into simulations in the form of the Drude model, the maximum modulation amplitude achieved during material evolution increases by approximately 10 times (solid line). The break in the line corresponds to the stage of the surface melting in both modulation minima and maxima, after which the surface layer experiences further heating. Interestingly, in modeling with the constant optical parameters (dashed line) the melting threshold was not reached (maximum surface temperature ~800 K), which contradicts the experimental observations (the ablation threshold of gold under the studied irradiation conditions is ~0.4 J/cm^2 [52]).

As mentioned above, the simulations with the constant optical parameters do not agree with the experimental value of the damage threshold fluence. The explanation is presented in Fig. 5.3c showing the dynamics of the laser light absorption [51]. As

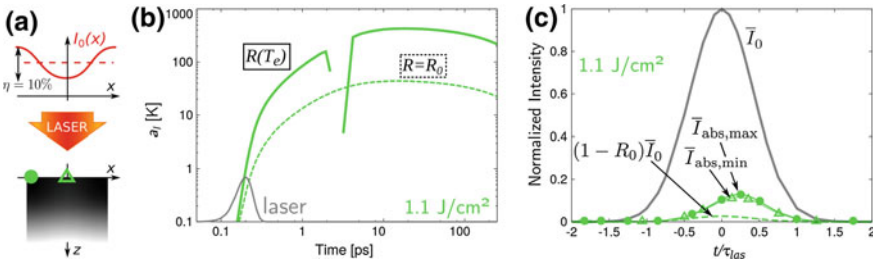

Fig. 5.3 **a** Schematics of the modeled problem on the temporal evolution of the modulated temperature profile generated by the periodically modulated laser intensity across the laser beam (adapted from [40]). It was assumed that the electromagnetic wave at the surface experiences 10% modulation as a result of the interference of the incident laser pulse and the surface scattered wave. **b** The modulation amplitude a_l as a function of time for laser-irradiated gold surface. The laser pulse parameters are: 800 nm wavelength, 100 fs pulse duration, laser fluence of 1.1 J/cm^2. The laser pulse profile is shown by grey line. The results of modeling with the constant and electron temperature dependent optical properties are presented by dashed and solid lines, respectively. **c** The simulated laser energy absorption by gold for the case given in (**b**). The temporal profile of the laser pulse is depicted by a grey solid line. The dashed green line corresponds to a simulation performed with the constant optical properties. Green solid lines are obtained for the temperature modulation maxima and minima with using the Drude model to describe the transient variation of optical properties of gold during and after the laser irradiation (highlighted by dots and triangles, respectively). All lines are normalized by the intensity maximum of the incident laser pulse. Panels (**b**) and (**c**) are adapted from [51]

the reflectivity of gold is very high at 800 nm wavelength (~97.5%), only a very small fraction of the beam energy is absorbed. When the dynamic change of the reflectivity is accounted for in the simulations, a considerably higher fraction of the laser energy is absorbed (green solid lines for the modulation maxima and minima highlighted by dots and triangles, respectively), thus leading to a reasonable agreement with the experimental observations [52]. An interesting feature of absorption can be noticed in Fig. 5.3c: the absorption maximum in gold is shifted toward the tail of the laser pulse, contrary to the case of dielectrics discussed in the next section.

5.2.2 Bandgap Materials

The wide bandgap dielectrics are transparent for light in visible and IR spectral ranges. The ultrashort pulse ablation in these wavelength ranges is achieved via nonlinear effects involving multiphoton or tunnelling ionization, which can be followed by collisional multiplication of free electrons effectively absorbing laser light (the so-called avalanche process). The details of numerical models for description of the processes excited in wide bandgap dielectrics can be found in [6, 53, 54] (see also Supplementary Materials for [54]). Here we only briefly focus on the variation of the optical properties of transparent materials under irradiation by powerful ultrashort

laser pulses. It is stressed, however, that in order to account for a correct description of ultrashort laser pulse interaction with bandgap materials via continuum-level modeling, these optical properties must be coupled to the description of the local beam intensity in the material. The latter can involve different levels of numerical description from the basic depletion of the laser intensity along its pathway by the different ionization and heating processes [54] to a full Maxwell model [55].

Spatiotemporal dynamics of the optical parameters in transparent dielectrics are well described within the Drude formalism via the complex dielectric function $\varepsilon(n_e)$ that accounts for the contributions from unexcited matter and generated dense plasma of free electrons [12]:

$$\varepsilon = 1 + (\varepsilon_g - 1)\left(1 - \frac{n_e}{n_{\text{val}}}\right) - i\frac{n_e e^2 \tau_c}{\omega \varepsilon_0 m_e^*(1 - i\omega\tau_c)} \tag{5.12}$$

(compare with (5.1)), where n_{val} is the total number of the valence electrons in the unexcited material and ε_g is its dielectric function. From this equation, we can introduce the critical electron density for bandgap materials $n_{cr} = \varepsilon_0 m_e^* R_e(\varepsilon_g)\omega^2/e^2$, at which the oscillation frequency of free electrons (or plasma frequency ω_p, see above) is in resonance with the electromagnetic wave frequency ω. The critical density n_{cr} is one of the fundamental parameters characterizing the interaction of electromagnetic waves with ionisable materials. Note that this value can differ from the critical plasma density in gas plasmas, which is equal to $\varepsilon_0 m_e \omega^2/e^2$. As soon as the condition $n_e > n_{cr}$ is reached for a particular light wavelength, free electron plasma strongly reflects such light. Equation (5.12) together with the Fresnel formulas are usually introduced to the models of laser excitation of bandgap materials based on the rate equations for the generation of free electrons. As noted above, the coefficient of light reflection from an inhomogeneous dense plasma at the sample surface layer should be calculated within a multilayer reflection model.

Figure 5.4 presents the simulation data for fused silica irradiated by 130 fs laser pulses at 800 nm wavelength [54]. It must be underlined that the damage threshold fluence predicted in the simulations (2.27 J/cm^2) is in excellent agreement with experimental measurements. It is observed that, as soon as the critical plasma density is exceeded in the surface layer of fused silica (Fig. 5.4a), the laser light start to be reflected from the metalized material surface (Fig. 5.4b). In this case the reflection is more efficient in the beam tail when the material becomes considerably ionized, contrary to laser excited metals, where light reflection is reducing in the second part of the laser beam (Fig. 5.3c). Interestingly, the mirror-like behavior of the ionized surface layer leads to an effective reduction of the duration of the laser pulse that penetrates into the sample. At the largest simulated fluence, as much as half of the laser beam energy is reflected from the surface. It must be also underlined that a noticeable part of the beam is transmitted through the transparent material even at the highest laser fluences studied in the simulations, mainly in the first half of the pulse duration. The same formalism can also be applied to semiconductor materials as discussed below.

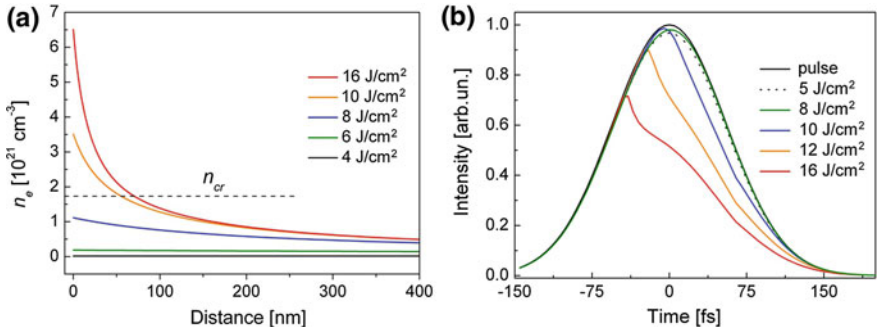

Fig. 5.4 **a** The spatial profiles of the free-electron density at a time of 100 fs after the maximum of the laser pulse with 130 fs duration and 800 nm wavelength. **b** Dynamic changes in the laser intensity of the beam entering the sample after its partial reflection from the laser-excited surface layer, $(1 - R(t)) \times I_0(t)$ where $I_0(t)$ and $R(t)$ are the incident laser intensity (black solid line) and the time-dependent reflection coefficient, respectively. Adapted from [54]

5.2.3 *Semiconductors: Non-thermal Melting and Pump-Probe Experiments*

In this section, we address the problem of theoretical description of time-resolved reflectivity measurements for silicon irradiated by ultrafast laser pulses. Although silicon is, for historical reasons, one of the most studied materials, the modeling of its nonequilibrium behavior upon intense laser irradiation remains challenging, particularly in the regime of material modification. For picosecond laser pulses of moderate intensity, when the free electron density remains considerably below the critical plasma density, the approach developed by van Driel based on the rate and energy balance equations [56] represents an excellent example of a successful numerical model. As soon as the free electron density produced by laser irradiation approaches the n_{cr} value, the transient optical properties of laser-excited silicon were found to be well described by an analogue of the Drude model, similar to (5.12) [57].

A sensitive method to study the thermodynamic pathways of matter out of equilibrium is to compute and compare the transient reflectivity dynamics obtained for a material in the pump-probe experiments. A pump laser pulse excites the material while a low-energy probe pulse is applied with a short variable delay to measure how the reflectivity evolves. The reflected probe beam contains information on the instantaneous state of the material through its optical properties. For silicon, an adequate computational description of the transient optical properties matching well the experimental data was achieved up to the melting threshold [12].

Well above the melting threshold fluence, close to 0.6 J/cm^2, the quantum-level effects triggered by the high level of excitation of the electron-hole pairs become dominant and substantially complicate the mathematical description of the laser-induced processes at large scale, particularly in 2D and 3D cases. As was found experimentally for semiconductors using time-resolved X-ray diffraction, excitation

of ~10% of the total density of the valence electrons to the conduction band is sufficient to induce a bond softening followed by the lattice structural change already at femtosecond time scale, usually with a delay of ~300–400 fs after the maximum of the laser pulse [58–60]. At the atomistic level, the excitation of a large number of electron-hole pairs leads to considerable change of the interatomic potential resulting in lattice disordering, called non-thermal melting. Such ultrafast process is observed primarily in solids with anomalous thermodynamic properties, which exhibit compaction upon melting [61, 62]. It happens in a thin electronically overexcited region at the material surface, up to several dozens of nanometers [60], which, however, is sufficient to strongly affect the transient reflectivity of the irradiated sample. Non-thermally molten material is brought in a highly stretched state (negative pressure) followed by material compaction, which results in the transition from non-thermal to thermal liquid state called liquid-liquid phase transition (LLPT) [62–64]. During this transition stage, which lasts few picoseconds, the free electron subsystem transfers the energy necessary to achieve the thermally molten state to the lattice.

The effects of non-thermal melting in laser-excited materials have extensively been studied for silicon by molecular dynamic simulations [65–70]. The theoretical description of non-thermal melting and associated change in the material reflectivity, suitable for incorporation into continuum-level models describing pump-probe experiments (e.g., [71]), remains a challenging task. So far, only a few simplified analytical models of the non-thermal melting have been proposed, and the description of this process remains rather phenomenological [72, 73]. Moreover, the change of reflectivity of a highly and swiftly excited semiconductor experiencing non-thermal melting includes not only the contributions from free-carrier density variation and state filling [74] but also bandgap shrinking and collapse [60, 75].

During the construction of the model of ultrashort laser excitation of silicon [76], two additional effects have been found to strongly affect the sample reflectivity. (i) When calculating the ambipolar diffusion of the electron-hole pairs, the use of the density-dependent electron-phonon coupling time [77] was found to provoke a transient melting in a sub-surface region that affects the phase detected by the probe pulse and leads to reflectivity oscillations on the picosecond timescale. As this effect was not observed experimentally, the coupling time in the over-dense region was limited to 2 ps, in accordance with time-dependent x-ray scattering experiments [78]. (ii) At relatively low fluences, but above the melting threshold, the transient melting can happen heterogeneously in a rather thick surface layer of silicon. For such a layer, the material refractive index can be described as a simple interpolation between the dielectric permittivity of the excited solid and the molten material permittivity. At high fluences, the transient melting is rather happening via formation of homogeneously distributed melting centers below the surface, as shown by molecular dynamics simulations [79]. The homogeneous melting can be accounted for in the description of the macroscopic optical properties in the framework of the Lorenz-Lorentz model of the effective medium [28], where a fraction of the material is a locally excited solid and another fraction is molten.

By applying the irradiation parameters described in [71] to the model, a good agreement was obtained with the experimental data on the transient pump-probe

reflectivity at 1 μm wavelength for the regimes below the melting threshold. For such irradiation parameters, when the reflectivity dynamics is governed by the response of the excited free electrons, the probe signal is reasonably well described by the Drude model in the form given by (5.12). Upon reaching conditions for thermal melting, the molten silicon starts to contribute to the reflectivity signal, and the model predictions deviate from the measurements. Evidently, an adequate model of homogeneous nucleation of the molten phase is required. However, the main feature of this regime, a swift increase of the reflectivity during the laser pulse due the free electron excitation followed by the reflectivity decrease attributed to the electron recombination and a new raise of reflection conditioned by thermal melting of the lattice, is qualitatively reproduced in the modeling. In the regimes of the non-thermal phase transition (at fluences 3–4 times exceeding the thermal melting threshold), the measurements do not reveal the stage of reflectivity decrease due to the electron recombination [71]. The reflectivity increase as a result of the bandgap collapse at the femtosecond time scale [60] has not yet been described in the large-scale numerical simulations. An adequate description of this effect calls for further model developments.

5.3 Continuum-Level Modeling of Thermal and Mechanical Response to Laser Excitation at the Scale of the Laser Spot

The laser excitation of the optically active states in the irradiated target followed by the initial ultrafast non-thermal material response to the electronic excitation and thermalization of the deposited laser energy, discussed in the previous section, set the stage for slower thermal and mechanical processes leading to material modification, redistribution, and removal/ablation. The understanding of these processes is critical for the advancement of laser applications based on material modification, selective removal and/or deposition. A set of computational techniques capable of revealing the information on the heat transfer, elastic and plastic deformation, phase transformations (melting, resolidification, vaporization and volume ablation processes), hydrodynamic flow of transiently melted material, and generation of unusual configurations of crystal defects are briefly reviewed in this section, with the focus on methods capable of addressing the processes occurring on the scale of the whole laser spot.

5.3.1 Thermal Modeling of Laser Melting and Resolidification

At the most basic level, computational description of thermal processes in laser-material interactions should account for the thermal energy redistribution and phase transformations in a region affected by the laser energy deposition. A continuum model based on the numerical solution of the heat diffusion equation complemented by source terms describing the laser energy deposition and the heat of melting/solidification can often serve as the first step in the analysis of the laser-induced processes. The simple thermal model can be expressed in this case by the following equation:

$$\rho C_p \frac{\partial T}{\partial t} = \nabla \cdot (K_{\text{th}} \nabla T) + S_{\text{laser}} - S_m - S_e, \tag{5.13}$$

where ρ, C_p, and K_{th} are the density, heat capacity, and thermal conductivity of the target material, respectively, and the three source terms on the right side of the equation represent the thermal energy sources/sinks due to the laser energy deposition, S_{laser}, the release/absorption of heat at melting/solidification front, S_m, and the energy loss through vaporization from the surface of the irradiated target, S_e. As discussed in Sect. 5.2, the spatial distribution of the laser energy deposition is defined by the optical properties of the material and the energy redistribution during the equilibration of the optically excited states, while the action of the other two source terms is spatially localized in the vicinity of the liquid-crystal interface and the surface of the target.

In the description of melting and resolidification, a simple phase-change model based on an assumption of local equilibrium at the solid-liquid interface (heat-flow limited interface kinetics formulated within the framework of the Stephan problem [80, 81]) is not suitable for the conditions of short pulse laser irradiation, when strong temperature gradients are created and fast thermal energy flow to/from the solid-liquid interface can lead to significant superheating/undercooling of the interface [82–86]. Therefore, a nonequilibrium kinetic description [86–88], in which the instantaneous velocity of the solid-liquid interface is defined by local temperature of the interface predicted by (5.13), is needed for a realistic representation of the movement of the solid-liquid interface. The temperature dependence of the velocity of the melting or solidification front can be described by a kinetic equation formulated as follows [86–88]:

$$V_i(T_i) = V_0(T_i)\left[1 - \exp\left(-\frac{\Delta G(T_i)}{k_B T_i}\right)\right], \tag{5.14}$$

where T_i is the temperature at the solid-liquid interface, $V_0(T_i)$ is a prefactor, and $\Delta G(T_i)$ is the difference in the Gibbs free energy between the liquid and crystalline phases. At small deviations from the equilibrium melting temperature T_m, the free energy difference can be approximated as $\Delta G(T_i) \approx \Delta H_m(T_i) \cdot (1 - T_i/T_m)$, where

$\Delta H_m(T_i)$ is the latent heat of solid-liquid phase transformation. The prefactor $V_0(T_i)$ can be fitted to the results of a series of solid-liquid coexistence atomistic simulations providing the temperature dependence of the interface velocity, as described in Sect. 5.4.1. Note that the decrease of the solidification velocity with increasing undercooling, predicted by (5.14) $V_0(T_i)$ decreasing with increasing undercooling [88], may permit the transformation of the undercooled liquid into a stable amorphous phase, which would stop the advancement of the crystallization front and result in the formation of amorphous regions in the resolidified target. The possibility of phase transformations occurring through the homogeneous nucleation of a new phase should also be included to account for the nucleation of liquid regions inside a crystal superheated up to the limit of its stability against melting [89–92] or homogeneous nucleation of new crystallites in a strongly undercooled molten part of the target [83–85, 93].

As an example of the application of the thermal model described above, we consider the results of a simulation of a silicon target irradiated by 30 ps laser pulse at an incident fluence of 0.3 J/cm^2 and a laser wavelength of 532 nm. The temperature and phase state evolution in the irradiated target is evaluated by solving (5.13 and 5.14) in cylindrical coordinates (r, z) and illustrated by a series of contour plots in Fig. 5.5. Short pulse laser irradiation results in a fast heating and melting of a surface region of the target, with the depth of melting reaching ~60 nm in the center of the laser spot. The laser heating and melting are followed by a rapid cooling and solidification, as can be seen from the upwards movement of the liquid-crystal interface shown in Fig. 5.5 by black lines. The solidification process proceeds through the epitaxial crystal regrowth, and the crystallization kinetics is described by (5.14) with parameters evaluated based the results of atomistic simulations discussed below, in Sect. 5.4.1. At the periphery of the laser spot, a lower energy density deposited by the laser pulse results in a rapid undercooling of the molten region down to temperatures below 0.71 T_m, where the atomic rearrangements become too sluggish for the advancement of the crystallization front (see Sect. 5.4.1). As a result, the advancement of the front at the periphery of the laser spot stops at ~1.5 ns, leading to the formation of stable amorphous phase. At the center of the laser spot, however, the temperature of the solidification front remains above the level required for the transition to the amorphous phase until the front reaches the surface of the target. As a result, a ring-shaped amorphous region surrounding the fully recrystallized central part of the laser spot is formed, as illustrated by Fig. 5.5f. The observation of the ring-shaped amorphous region is consistent with experimental observations for silicon targets irradiated by a single 30 ps laser pulse [94] or by several 100 fs laser pulses [95].

The rapid solidification proceeding under conditions of strong undercooling may produce a high density of crystal defects, such as vacancies, interstitials, dislocations, twin and grain boundaries. In particular, as suggested by the results of atomistic simulations discussed in Sect. 5.4.1, a high concentration of point defects (vacancies and interstitials) can be generated in short pulse laser-induced melting and resolidification of metals and semiconductors. In order to investigate the distribution of point defects on the scale of the laser spot, the predictions of the atomistic simulations can be utilized to design and parametrize a continuum-level description of

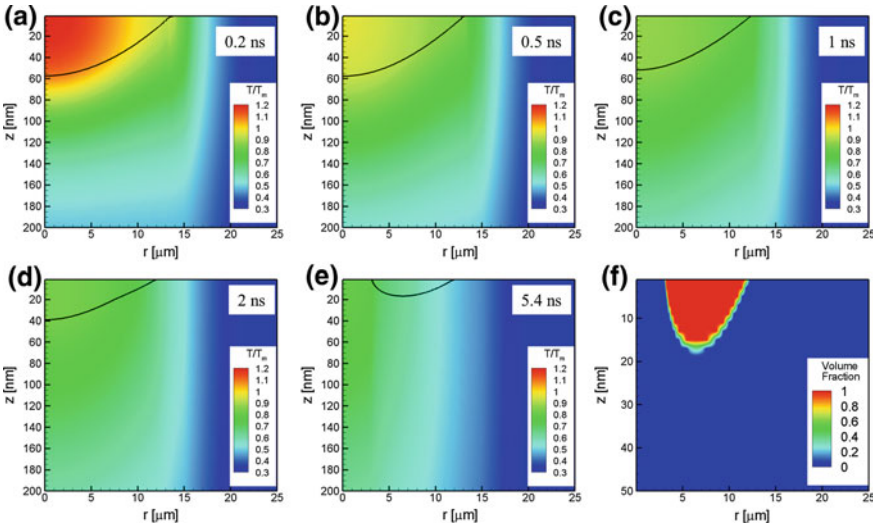

Fig. 5.5 Computational predictions of temperature evolution **a**–**e**, and formation of a ring-shaped amorphous region **f** in the surface region of a Si target irradiated by a 30 ps laser pulse at an incident fluence of 0.3 J/cm^2 and a laser wavelength of 532 nm. Figures **a**–**e** show the contour plots of temperature distribution at different time after the laser irradiation. The simulation is performed for 5.4 ns, until the end of the resolidification process. The black lines show the location of the interface between the crystalline and molten/amorphous parts of the target. Figure **f** demonstrates the spatial distribution of a volume fraction of the amorphous phase, formed by 5.4 ns due to fast cooling of the molten region. Note that in (**f**) the scale in z direction is different from (**a**)–(**e**)

the generation of point defects within the general framework of the thermal model discussed above. Equations (5.13 and 5.14) can be complemented with the following equations accounting for the generation, diffusion, and recombination of vacancies and interstitials in the irradiated target [96–99]:

$$\frac{\partial C_I}{\partial t} = \nabla \cdot (D_I \nabla C_I) + K_{IV}\left(C_I^{\mathrm{eq}} C_V^{\mathrm{eq}} - C_I C_V\right) + S_I, \tag{5.15}$$

$$\frac{\partial C_V}{\partial t} = \nabla \cdot (D_V \nabla C_V) + K_{IV}\left(C_I^{\mathrm{eq}} C_V^{\mathrm{eq}} - C_I C_V\right) + S_V, \tag{5.16}$$

where D_I and D_V are the diffusion coefficients of interstitials and vacancies, respectively, K_{IV} is the interstitial-vacancy recombination rate, C_I, C_V, C_I^{eq}, and C_V^{eq} are the current and equilibrium concentrations of interstitials and vacancies, S_I and S_V are the source terms describing the generation of interstitials and vacancies at the propagating solidification front. The parameters of the model can be obtained from atomistic simulations, such as the ones discussed in Sect. 5.4.1.

The ability of the model implementing (5.13–5.16) to predict the distribution of point defects in a laser-processed target is exemplified in Fig. 5.6, which shows concentrations of interstitials and vacancies produced in the silicon target irradiated by a

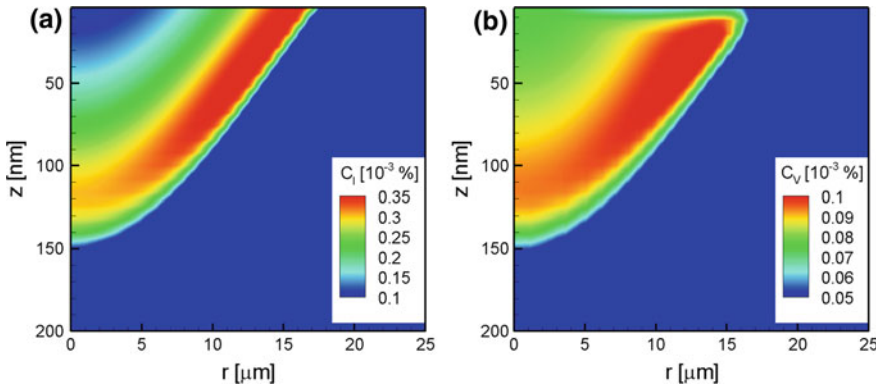

Fig. 5.6 The regions with high concentration of point defects produced in a single crystal Si target irradiated with a single 1 ns laser pulse at an incident fluence of 0.6 J/cm^2 and a laser wavelength of 532 nm. Spatial distributions of interstitials (**a**) and vacancies (**b**) are plotted at a time of 20 ns, after complete recrystallization of the target, and the scale is shown in units of atomic percent. The generation of point defects at the solidification front is parameterized based on the results of atomistic simulations, as discussed in Sect. 5.4.1

nanosecond laser pulse. In contrast to the simulation of picosecond laser irradiation discussed above and illustrated by Fig. 5.5, the irradiation by a longer, 1 ns, laser pulse decreases the temperature gradients and cooling rate, and does not result in the formation of amorphous phase. The substantial undercooling in the vicinity of the solidification front, however, leads to the formation of distinct regions of strong supersaturation of both vacancies and interstitials in the parts of the transiently molten region where the maximum undercooling was achieved. At later stage of the solidification process, the interfacial temperature increases due to release of the latent heat, and, as suggested in Sect. 5.4.1, the temperature increase from 0.91 to 0.95 T_m results in decreasing levels of vacancy and interstitial concentrations.

5.3.2 *Thermoelastic Modeling of the Dynamic Evolution of Laser-Induced Stresses*

The fast rate of energy deposition in short pulse laser processing applications may result not only in the rapid melting and resolidification of a surface region of an irradiated target but also lead to the generation of strong stresses within the absorption region. The laser-induced stresses are particularly high in the regime of stress confinement [100–103], when the time of the laser heating (defined by the laser pulse duration, τ_p, or the time of the electron–phonon equilibration, $\tau_{e\text{-}ph}$, whichever is longer) is shorter than the time required for the mechanical relaxation (expansion) of the heated volume, $\tau_s \sim L_p/C_s$, where C_s is the speed of sound in the target material and L_p is the effective depth of the laser energy deposition. The relaxation of the

initial compressive stresses generated by the laser energy deposition can result in the emergence of an unloading tensile component of the stress wave that is sufficiently intense to cause the formation subsurface voids [83, 104–107] or separation of a surface layer from the target in a process commonly called photomechanical spallation [100–103]. At lower laser fluences, the relaxation of laser-induced stresses in the vicinity of a free surface of the target can result in the co-emission of longitudinal, shear, and surface acoustic waves that can be utilized in many practical applications, including nondestructive evaluation of mechanical properties and surface defects [108–110], acoustic desorption [111–115] , and acoustic activation of surface diffusion [116–118].

The computational description of the dynamic evolution of thermoelastic stresses and the emission of stress waves can be described in the framework of the thermoelasticity model [43, 119–122], which complements the thermal model described above with the thermoelastic wave equation:

$$\rho \frac{\partial^2 u_i}{\partial t^2} = \frac{\partial \sigma_{ij}}{\partial x_j} = C_{ijmn}\left[\frac{\partial^2 u_m}{\partial x_j \partial x_n} - \delta_{mn}\alpha_L \frac{\partial T}{\partial x_j}\right], \tag{5.17}$$

$$\sigma_{ij} = C_{ijmn}\left[\frac{\partial u_m}{\partial x_n} - \delta_{mn}\alpha_L (T - T_0)\right], \tag{5.18}$$

where T, u_i, σ_{ij}, α_L, and C_{ijmn} are temperature, displacement, stress tensor, linear thermal expansion coefficient, and stiffness tensor, respectively. The transient heating/cooling induced by adiabatic compression/expansion of the material during the wave propagation can be accounted for by including an additional source term in the form of $-\alpha_L T C_{iimn} \frac{\partial^2 u_m}{\partial t \partial x_n}$ to the heat diffusion equation, (5.13). In literature, the stress tensor is commonly formulated for the case of isotropic material [120, 123]:

$$\sigma_{ij} = \delta_{ij}\lambda \cdot \left(\frac{\partial u_k}{\partial x_k}\right) + \mu \cdot \left(\frac{\partial u_i}{\partial x_j} + \frac{\partial u_j}{\partial x_i}\right) - 3\delta_{ij} B \alpha_L (T - T_0), \tag{5.19}$$

where $\lambda = B - 2G/3$ and $\mu = G$ are Lamé constants, B and G are bulk and shear moduli of the material. This formulation of the thermoelasticity model is suitable for the description of an irradiation process not only in Cartesian but also in cylindrical coordinates [123]. Equation (5.19), however, is not valid for description of highly anisotropic materials, e.g., single crystal silicon, where the description provided by (5.17 and 5.18) has to be applied.

The capabilities of the thermoelasticity model are illustrated in Fig. 5.7, which provides a snapshot of laser-generated elastic waves in a silica glass plate. The simulation is performed for an absorbed fluence of 10 J/cm^2, a laser spot size of 21 μm, and the characteristic absorption depth assumed to be 10 μm based on the depth of grooves observed in experiments. This simulation is motivated by an intriguing experimental observation of the spatial distribution of laser-induced damage in a silica glass plate undergoing laser cutting [124]. This study demonstrates the generation of damage lines on the rear surface of the plate, which are located not directly

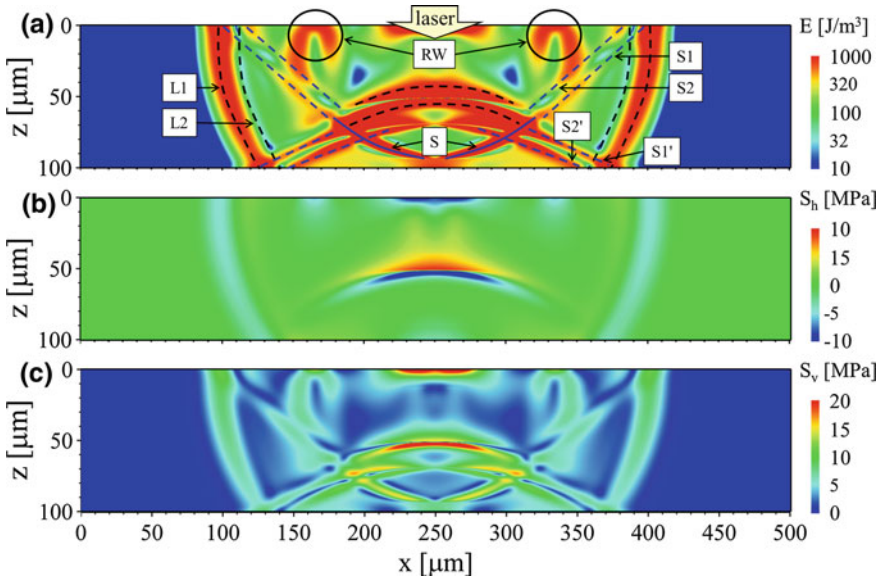

Fig. 5.7 Generation of elastic waves in a silica substrate irradiated by a laser pulse at 10 J/cm^2. The energy density (**a**), hydrostatic stress (**b**), and Von-Misses stress (**c**) are plotted for a time of 25 ns after the laser pulse. In **a**, the longitudinal and shear waves are schematically outlined by black and blue lines, respectively. Rayleigh waves, longitudinal compressive, longitudinal tensile, and shear waves generated by rapid laser heating are marked as RW, L1, L2, S, respectively. Shear waves emitted due to interaction of L1 and L2 waves with top and bottom free surfaces are marked as S1, S2, S1′, S2′. By the time of 25 ns, L1 and L2 waves are already reflected from the bottom free surface and propagate upwards. The thermal stresses generated by laser heating cannot be completely relaxed by the material expansion towards the free surface and, therefore, are still present in the vicinity of the irradiated area

underneath the laser spot but at ~37° angle. The rear surface damage is attributed in [124] to the interaction of a shear wave emitted from the irradiated spot and a surface Rayleigh wave generated due to reflection of a longitudinal wave from the rear surface. To verify this hypothesis, thermoelasticity modeling of the generation of stress waves in a silica glass substrate is performed in Cartesian coordinates for a two-dimensional geometry. Laser-induced heating of the target triggers generation of a variety of acoustic waves that interact with the free surfaces of the silica glass plate and create a complex dynamic pattern of transient stresses within the plate, as depicted in Fig. 5.7. The calculations, however, do not support the original explanation of the rear surface damage suggested in [124], as the reflection of the longitudinal waves from the bottom surface of the plate does not produce Rayleigh waves of any significant magnitude. Therefore, an alternative explanation of the experimental observations is needed.

5.3.3 Material Redistribution Through Elastoplasticity and Hydrodynamic Flow

The generation of strong thermoelastic stresses can not only lead to the emission of elastic waves and photomechanical damage but can also result in material redistribution within the laser spot or removal from the target. In particular, the relaxation of laser-induced stresses plays a major role in the laser-induced forward transfer (LIFT) [125–128] and thin film patterning/scribing [93, 129–131], where the initial motion of the film driven by the laser-induced stresses defines to a large extent the final outcome of the target modification and/or parameters of the ejected material. The computational analysis of laser interactions with thin films has been performed with both atomistic [93, 131, 132] and continuum [122, 123, 133] models, and has provided important insights into the complex interplay between the dynamic relaxation of laser-induced stresses, phase transformations, and material redistribution/removal.

As an example of continuum simulation of LIFT, the results of a simulation of the forward transfer of a SnO_2 film deposited on a silica or a polymer substrate and irradiated by a nanosecond laser pulse are illustrated by Fig. 5.8. Two dimensional finite element formulation of the elasticity equation in cylindrical coordinates is applied to study the initial stage of LIFT process involving delamination of the film from the donor substrate and formation of a microbump [122]. The simulation is performed in the irradiation regime where the vaporization of the film material is negligible, and the film dynamics is governed mainly by mechanical processes. The temperature increase predicted by the thermal model is used to calculate the initial distribution of elastic stresses, and the following evolution of the film is described by solving the elasticity equation.

The effect of the substrate elastic properties on the initial stage of LIFT process is assessed by performing simulations for silica and polymer substrates, as shown in Fig. 5.8. Heating the film leads to initiation of a bending wave near the edges of the irradiated spot that propagates in the film and collapses at the center of the spot. According to Fig. 5.8c, three stages of the film detachment can be distinguished in the case of silica substrate: increase of the wave amplitude (1), wave propagation (2), and the final swift uplifting of the central part of the film (3). The simulations reveal a remarkable fact that both the wave amplitude and the velocity component of the film motion at the wave peak are increasing with propagation of the wave toward the center. In the case of the polymer substrate, however, the film has a possibility to expand not only in the direction of the free boundary but also partially toward the donor substrate, compressing the latter. This lowers the stress value at the edges of the spot and, thus, prevents the formation of large velocity gradients normal to the substrate. Therefore, the film is separated uniformly and gently transferred to the acceptor, mitigating damage to the receiver substrate.

For longer laser pulses, outside the regime of stress confinement, the relaxation of thermoelastic stresses takes place during the laser energy deposition, and the processes that control the material response to the laser irradiation are largely of thermal nature and include melting, evaporation from the surface, and, at high laser intensi-

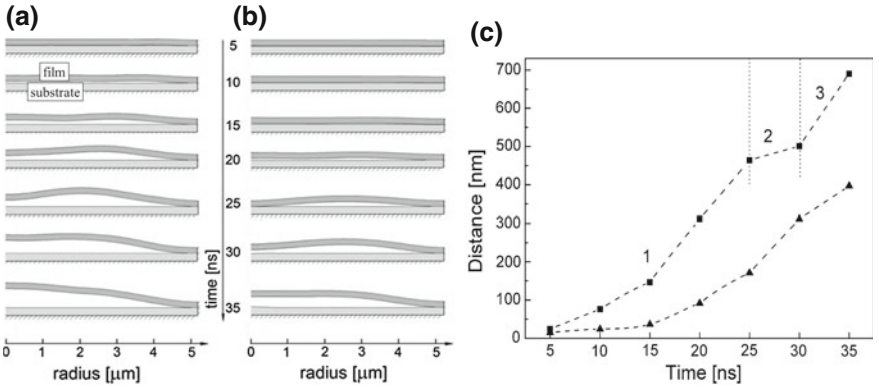

Fig. 5.8 Stages of a 250 nm SnO_2 film deformation demonstrating the initiation of a bending wave at the edge of the irradiation spot followed by detachment of the film from a silica (**a**) and a polymer (**b**) substrates. The maximum distance between the film and the substrate as a function of time (**c**) is shown by squares for the silica and triangles for the polymer substrates. The following stages of the film detachment are identified: increase of the wave amplitude (1), wave propagation (2), and the final swift uplifting of the central part of the film (3). The images are adapted from [122]

ties, a volumetric ablation through phase explosion, or explosive boiling [134–136]. The melt dynamics induced by pressure gradients, however, can still play an important role in laser processing even for continuous wave (CW) laser irradiation. In particular, the melt expulsion from the center of the laser spot is one of the primary mechanisms of CW laser damage and material removal [137–140]. The two main driving forces responsible for melt expulsion are the recoil pressure created by the evaporation process and the Marangoni effect. The melt expulsion by the recoil pressure is caused by the spatial variation of the vapor pressure within the laser spot [141–143], whereas the Marangoni effect is related to the variation of the surface tension along the non-uniformly heated surface of the molten pool [144, 145].

Computationally, the melting, evaporation, and melt flow in the course of material processing by long laser pulses can be described in hydrodynamic simulations based on the solution of Navier-Stokes equations [146]. In particular, the relative contributions of the recoil pressure and Marangoni effects to the CW laser melting and damage of aluminum films have been studied for a broad range of process parameters realized in both laser damage and material processing applications [146]. The simulations, performed with a two-phase hydrodynamic model, reveal only a marginal effect of the Marangoni stresses on the overall picture of melt flow and the melt-through time. The recoil pressure effect, on the contrary, is found to be capable of strongly decreasing the melt-through time in a certain range of laser intensity. Moreover, at high laser intensities, the surface of the molten pool can become unstable with respect to the appearance of waves propagating towards the edge of the molten pool, as illustrated in Fig. 5.9. The formation of waves on the surface of the molten pool and their interaction with the edge of the pool can produce an irregular complex shape of the rim of resolidified material commonly observed around the

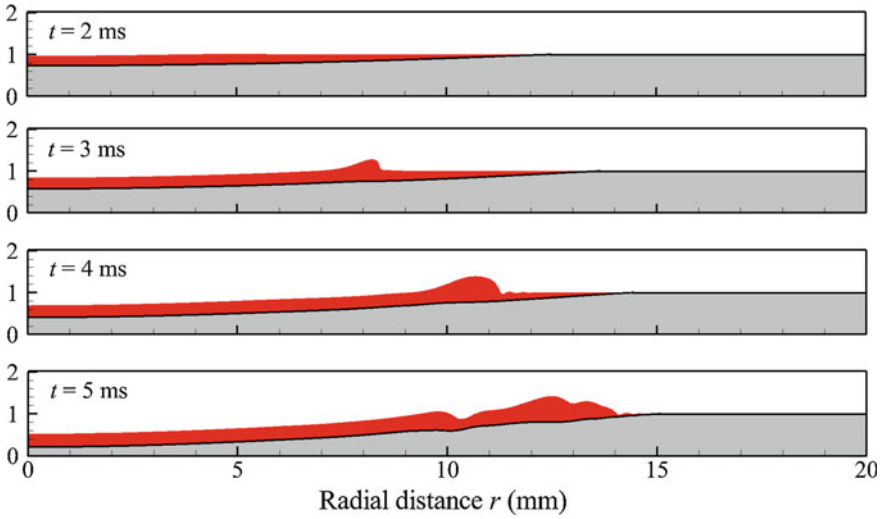

Fig. 5.9 The evolution of the shape of the molten pool (red region) in laser melting of a 1-mm-thick aluminum film irradiated by a CW laser with intensity of 3×10^6 W cm^{-2} and FWHM laser spot radius of 1 cm. The snapshots from the simulation are taken at times t after the start of the laser irradiation shown on the frames. The gradient of the recoil pressure within the laser spot induces fluid flow in the radial direction and leads in the appearance of a wave propagating towards the edge of the molten pool. The melt expulsion has a strong effect on the melt-through time of the free-standing film. The image is adapted from [146]

"crater" generated in the central part of the laser spot by the melt expulsion and active evaporation [138–140].

5.4 Molecular Dynamics Modeling of Laser-Materials Interactions

The brief overview provided in Sect. 5.3 demonstrates the ability of the continuum-level models to provide a computationally-efficient description of a broad range of laser-induced thermal and mechanical processes at experimental time- and length-scales. The predictive power of the continuum methods, however, is limited by the need for a priori knowledge of all processes that take place under given irradiation conditions and the availability of reliable mathematical description of these processes. The complexity and highly nonequilibrium nature of laser-induced processes, particularly in the short-pulse laser irradiation regime, can challenge some of the key assumptions of the continuum models and calls for complementary approaches that may help to design and verify the continuum models.

The atomistic modeling based on the molecular dynamics (MD) simulation technique is capable of providing atomic-level insights into the laser-induced processes

and is well suited for the exploration of complex nonequilibrium processes and for revealing new physical phenomena [4, 5, 7, 147]. The main advantage of the MD technique is that the only input into the model is the description of interatomic interactions, and no assumptions are made on the processes or mechanisms under study. This advantage, however, comes at a price of a high computational cost, which imposes severe limitations on the time- and length-scales accessible for MD simulations. It is not common to perform simulations for systems with sizes exceeding a few hundreds of nanometers (10^8–10^9 atoms) and to follow the evolution of a model system for times longer than several tens of nanoseconds. The direct MD simulation of processes occurring on the scale of an entire laser spot with a typical diameter of tens to hundreds of micrometers is clearly out of reach even with the most powerful modern supercomputers. Nevertheless, the processes occurring at the scale of the whole laser spot can still be investigated by combining results of MD simulations performed at different local laser fluences and mapping them to different locations within the laser spot [79]. More importantly, the new physical insights into the fast nonequilibrium processes, provided by MD simulations, can serve as the basis for the design of advanced continuum-level models fully accounting for the complexity of short pulse laser-materials interactions. Several examples illustrating the ability of MD simulations to reveal the processes contributing to material modification by short laser pulses are provided below.

5.4.1 Molecular Dynamics: Generation of Crystal Defects

The ability of short pulse laser irradiation to produce high densities of crystal defects and unusual defect configurations has been demonstrated in a number of large-scale MD simulations [83–86, 148, 149]. In particular, the simulations reveal the mechanisms responsible for surface nanocrystallization [83, 93, 147], generation of unusual metastable phases [149], high densities of dislocations, twin boundaries, and vacancies [83, 84, 86, 148]. Two examples discussed in this section are chosen to illustrate the application of MD simulations for parametrization of continuum-level models and for revealing new mechanisms of microstructure modification activated by short pulse laser irradiation.

As discussed in Sect. 5.3.1, the continuum-level simulations of laser melting and resolidification of silicon substrate can predict the morphology of amorphous phase and the distribution of point defects in the region of a target modified by laser irradiation. These predictions, however, rely on the availability of a kinetic model for the temperature dependence of the solidification front propagation, conditions for the formation of a stable amorphous phase, and the generation of crystal defects in the solidification process. Under conditions when direct experimental probing of the rapid nonequilibrium phase transformations and generation of crystal defects in short pulse laser processing remains challenging, the MD simulations can provide the information needed for the design of continuum models.

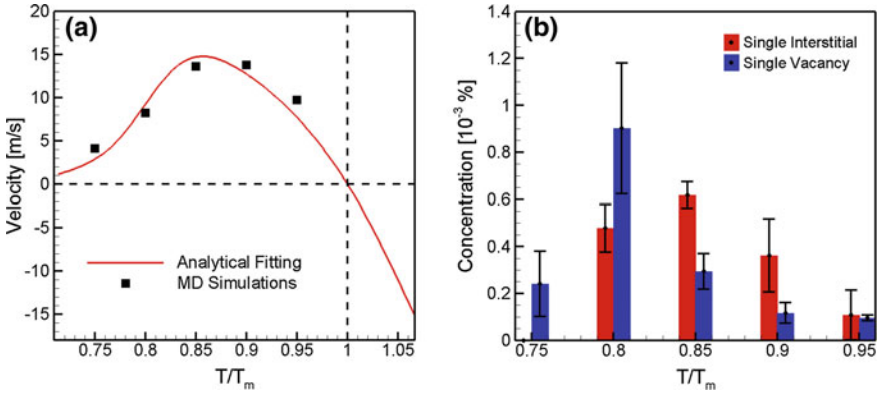

Fig. 5.10 Velocity of the crystal-liquid interface as a function of temperature (**a**), and concentration of point defects generated during solidification (**b**) predicted in MD simulations of a two-phase crystal-liquid Si system with a (100) orientation of the crystal-liquid interface under constant temperature and zero pressure. In **a**, the black squares show the velocity of the solidification front predicted in MD simulations, and the red line depicts fitting of (5.14) to the MD results. In **b**, the red and blue bars represent the concentration of single interstitials and vacancies, respectively, averaged over four simulations performed under the same conditions. The black bars show the standard deviation of the mean calculated based on the four simulations

This application of MD model is illustrated in Fig. 5.10 that shows the temperature dependence of the velocity of the solid-liquid interface and the concentration of point defects generated in silicon undergoing rapid solidification at different levels of undercooling below the equilibrium melting temperature. The simulations start from a solid-liquid coexistence system and are performed under constant undercooling and zero external pressure. The velocity of the epitaxial growth of a (100) crystal-liquid interface is evaluated at different temperatures, and the results are used to define the parameters of the analytical dependence given by (5.14), as shown in Fig. 5.10a. The analysis of the resolidified parts of the system reveals that a substantial number of individual point defects and their clusters are generated in the rapid solidification process. The concentrations of single interstitials and single vacancies are averaged over four simulations performed under the same undercooling conditions, and the results are shown in Fig. 5.10b as a function of temperature. The generation of clusters of point defects is not observed in simulations performed at temperatures higher than $0.9\,T_m$. The computational predictions on the concentrations of vacancies and interstitials left behind the rapidly advancing solidification front are used for parametrization of the corresponding source terms in (5.15) and (5.16) used in the continuum-level modeling of the laser-induced generation of crystal defects in silicon targets (see Sect. 5.3.1).

The MD method has also been successfully applied to explain recent electron backscatter diffraction measurements [150], which demonstrated strong effect of the crystallographic orientation of grains in polycrystalline metal targets on the generation and accumulation of crystal defects in the surface region of the irradiated

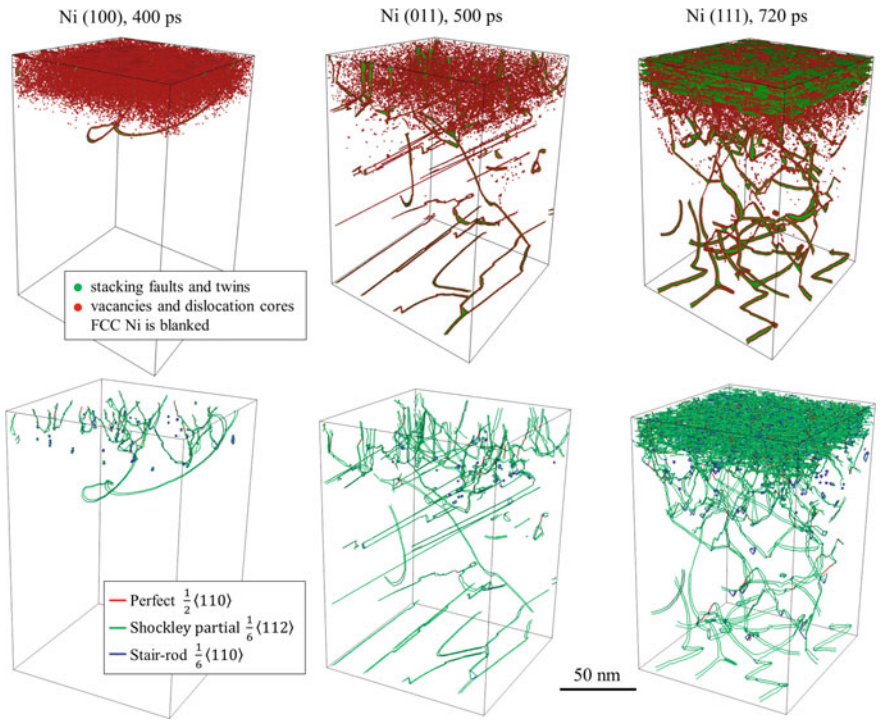

Fig. 5.11 The defect configurations predicted in TTM-MD simulations of (100), (011), and (111) Ni targets irradiated by a 50 fs laser pulse at an absorbed laser fluence of 60 mJ/cm^2. The top row depicts atomic configurations where only the atoms that belong to crystal defects are shown and are colored based on the local structure environment. The bottom row shows the dislocation configurations, with dislocations colored based on their type. The configurations are shown after complete resolidification of the targets

material. In order to adapt the classical MD method for simulation of laser interaction with metals, the description of the laser excitation of the conduction band electrons, electron-phonon coupling, and electronic heat conduction is incorporated into the model by combining MD with TTM discussed above, in Sect. 5.2.1. The results of large-scale atomistic simulations performed with the combined TTM-MD model [151] for Ni targets with (001), (011), and (111) surface orientations confirm the significant influence of the crystal orientation on the formation of sub-surface defects and provide detailed information on the defect configurations generated in each target, as shown in Fig. 5.11.

The results of the simulations also reveal the mechanisms responsible for the generation of dislocation in the three targets. The fast laser heating and the corresponding stresses generated in the surface region of the irradiated targets result in the emission of numerous Shockley partial dislocations in targets with (011) and (111) surface orientations, with the latter exhibiting the highest density of disloca-

tions activated in 3 different {111} slip planes and interacting with each other to produce complex dislocation reactions. In the case of (100) target, however, even though the thermal stresses have approximately the same magnitude as for (011) and (111) surface orientations, the shear stress resolved on existing slip systems does not reach the critical value required for the onset of dislocation emission. In addition to the prompt dislocation emission during the dynamic relaxation of laser-induced stresses, the generation of dislocation loops and other crystal defects takes place during the resolidification of the transiently melted top regions of the irradiated targets. In particular, even though no dislocation emission is observed in the simulation with (100) surface orientation during the initial dynamic relaxation of the laser-induced stresses, a number of dislocations are generated in this system during the following propagation of the solidification front. In all simulations, the rapid advancement of the solidification front results in the generation of a high concentration of vacancies in the resolidified region, which can reach the level of 10^{-3} of the lattice sites, as can be seen from the upper row of snapshots shown in Fig. 5.11.

One notable effect that is only observed in a course of the epitaxial resolidification of the target with (111) surface orientation is the formation of a high density of coherent twin boundaries, $\Sigma 3$ {111}, at the final stage of the solidification process [86], as shown in Figs. 5.11 and 5.12. The initial stage of the resolidification process proceeds by the epitaxial regrowth of the crystal. The defect structure of the resolidified region, however, changes abruptly when the temperature at the solidification front drops down to about 0.86 T_m, and a large number of coherent twin boundaries appear in the planes parallel to the advancing (111) crystal-liquid interface. The depth of the region affected by the growth twinning as well the thickness of twined domains predicted in atomistic simulation are in a good quantitative agreement with the results of experimental study, as can be seen from the comparison of images shown in Fig. 5.12b, c.

To predict the dependence of the thickness of the surface layer affected by the growth twinning on laser fluence, a series of continuum-level simulations are performed with the TTM enhanced with a description of nonequilibrium melting and solidification [86]. The dependence of the velocity of solidification front calculated in MD simulations and the threshold temperature corresponding to the onset of growth twining are used to parametrize the continuum-level model. The predicted evolution of temperature, melting depth, and depth affected by growth twinning is shown in Fig. 5.12d. This example demonstrates the utility of a multiscale approach that eliminates the need to perform a series of computationally-expensive MD simulations for each set of conditions.

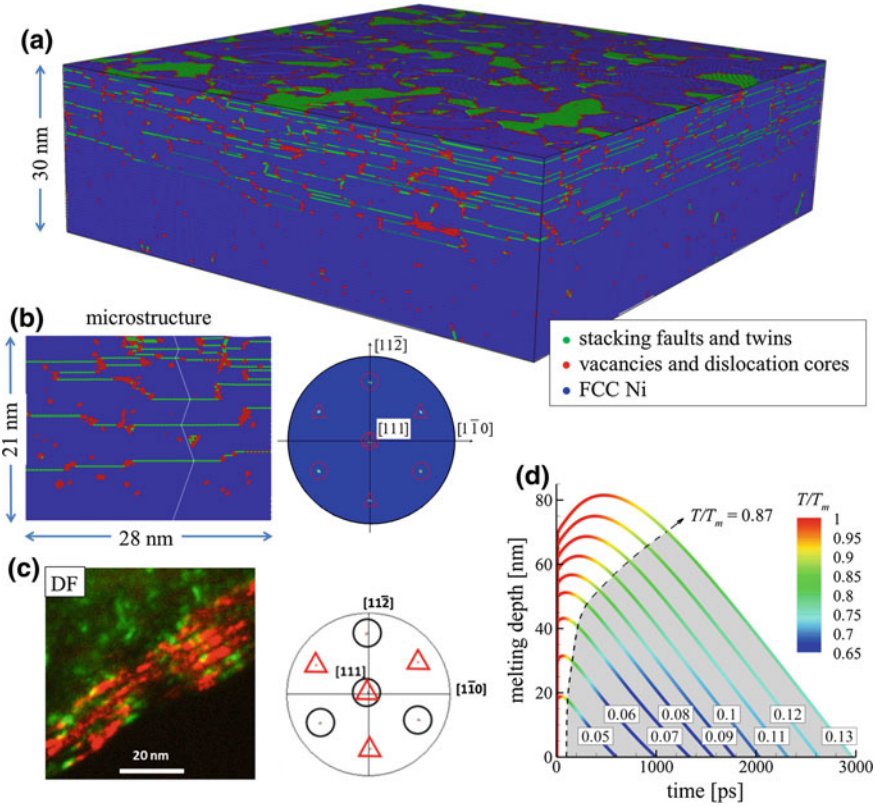

Fig. 5.12 Atomic configuration generated in a TTM-MD simulation of Ni (111) target irradiated by a 50 fs laser pulse at an absorbed laser fluence of 60 mJ/cm^2 (**a**), a representative vertical cross-section of the surface layer of the resolidified target and ⟨111⟩ pole figure calculated for 20 nm top region of the target (**b**), experimental results confirming the presence of twinned domains in the surface region of laser-processed Ni (111) target (**c**), and the evolution of the melting depth and temperature predicted in a series of continuum-level simulations parametrized based on MD results (**d**). In **a**, only a top 30 nm surface region is shown, and atoms are colored according to the local crystal structure environment. In **b**, the dashed white line shows the altering orientation of atomic planes in the twinned domains in the left panel, and the original and new/twinned ⟨111⟩ axes are marked by circles and triangles, respectively, in the pole figure shown in the right panel. In **c**, transmission electron microscopy (TEM) dark field images of the central part of the irradiated laser spot are superimposed to produce a false color image highlighting the spatial distribution of the epilayers (green) and twinned domains (red) in the left panel, while electron backscatter diffraction (EBSD) indexed crystal orientations are plotted in the ⟨111⟩ pole figure shown in the right panel. In **d**, the gray region corresponds to the conditions of strong undercooling ($T < 0.87\ T_m$), when the growth twinning is predicted in the theoretical analysis and atomistic TTM-MD simulations; different curves correspond to the different values of absorbed laser fluence marked in the plot in units of J/cm^2. The images are adapted from [86]

5.4.2 *Molecular Dynamics: Ablative Generation of Laser-Induced Periodic Surface Structures*

As already discussed above, the direct modeling of processes occurring on the scale of an entire laser spot is not feasible with MD method, and the results of the atomistic modeling can either be used for parametrization of a continuum model (e.g., see Sect. 5.3.1) or mapped to different locations within the laser spot, thus producing a "mosaic" view of processes occurring at different local fluences deposited within the spot by the (typically Gaussian) laser beam [79]. The latter approach, however, cannot account for the long-range lateral (parallel to the surface) redistribution of the molten material within the laser spot and the formation of large-scale surface topography frozen in during resolidification. Thus, in general, the analysis of the lateral flow in the molten pool remains squarely in the domain of continuum-level models, as illustrated in Fig. 5.9 and discussed in Sect. 5.3.3. Only in special cases of strong localization of the laser energy deposition down to submicron dimensions produced, e.g., through tight focusing of the laser beam [152–155], local field enhancement in the vicinity of a tip of a scanning probe microscope [156–159], or interference of multiple laser beams [160, 161], large-scale MD simulations can be directly used for investigation of the formation of frozen surface features in the course of the laser-induced lateral material redistribution [93, 131, 160–162]. One example illustrating the ability of MD simulations to provide a complete picture of the complex dynamic processes leading to the submicron surface patterning is discussed below for the single-pulse generation of LIPSS in the regimes of strong ablation [163] .

As discussed above, in Sect. 5.2.1, the formation of LIPSS is related to the dynamic optical response of the irradiated material to the ultrashort laser excitation, when the interference of the incident laser wave and surface electromagnetic wave produces spatial modulation of the laser energy deposition [45, 164]. Typically, LIPSS are produced by repetitive irradiation of the same area by multiple laser pulses with relatively low laser fluence, in the regime of surface melting and resolidification [164–168]. It is generally believed that an increase of the laser fluence well above the ablation threshold would result in disordering or even complete erasure of the periodic structures by the recoil pressure of the ablation plume. A number of recent studies, however, have demonstrated that the formation of high-quality LIPSS is possible in the single pulse irradiation regime at laser fluences well above the ablation threshold [47, 169–171].

In order to establish the mechanisms of the single pulse ablative LIPSS formation, a large-scale TTM-MD simulation has been performed for a Cr target irradiated by a 200 fs laser pulse [163]. The irradiation is assumed to produce a spatially modulated energy deposition arising from the interference of the incident laser wave and surface electromagnetic wave. The period of the sinusoidal modulation is taken to be 260 nm, and the maximum and minimum of absorbed fluences are 2000 and 3000 J/m^2 respectively, which corresponds to 20% modulation of the laser energy deposition with respect to the average level of 2500 J/m^2. The latter is approximately 70% above the phase explosion threshold for Cr target. The initial dimensions of the

TTM-MD domain are 260 nm × 43 nm × 87 nm, which corresponds to 81 million atoms, and the longest dimension matches the period of the laser energy deposition profile.

The response of the Cr target to the modulated laser energy deposition is illustrated in Fig. 5.13, where a series of snapshots of atomic configurations obtained in the simulation is shown up to 2100 ps after the laser pulse, when the surface of the target completely solidifies. The simulation reveals that the fast heating of Cr target by the laser pulse leads to an explosive decomposition of about 30–40 nm deep surface layer into a mixture of vapor and liquid droplets. Lateral pressure gradients in the plume generated by the spatially modulated laser ablation drive the vapor and liquid droplets to the region located above the minima of the laser energy deposition at the target surface. The material redistribution leads to formation of a high-density region evolving into an elongated liquid wall extending up to ~600 nm above the surface of the target. The upper part of the liquid wall disintegrates into droplets while the base of the wall solidifies on the timescale of ~2 ns, producing a ~100-nm-long frozen surface feature. Interestingly, while the amount of material removed from the trough area of the modified surface corresponds to the ablation depth of ~40 nm, the frozen surface protrusion extends above the level of the original surface of the target marked by dashed rectangles in Fig. 5.13. This computational prediction is consistent with the results of experimental study of the single-pulse LIPSS formation on Au surface [170, 172], where frozen wall-like structures, similar to those shown in Fig. 5.13, are observed. The computational insights into the LIPSS formation mechanisms may help in designing approaches for increasing the processing speed and improving the quality of the laser-patterned periodic surface structures.

5.5 Concluding Remarks

The overview of the diverse range of theoretical and computational approaches to the description of laser-materials interactions provided in this Chapter illustrates the ability of the advanced computational methods to provide a reliable description of different facets of these complex phenomena. In particular, while further advances in the theoretical treatment of the optical response of electronically-excited materials are certainly desired, the current models reviewed in Sect. 5.2 do provide a description of the transient variation of the optical properties of metals, semiconductors, and dielectrics excited by the laser irradiation that is sufficiently accurate for reliable evaluation of the fraction of the incident laser energy absorbed by the target, as well as spatial distribution of the deposited energy within the target. Similarly, the continuum-level models are capable of predicting the temperature evolution, elastic and plastic deformation, generation of stress waves, phase transformations (melting, resolidification, amorphization, vaporization, and volume ablation processes), hydrodynamic flow of transiently melted material, and generation of crystal defects on the macroscopic scale of the whole laser spot, as illustrated by several examples discussed in Sect. 5.3. Finally, the large-scale atomistic modeling has been demon-

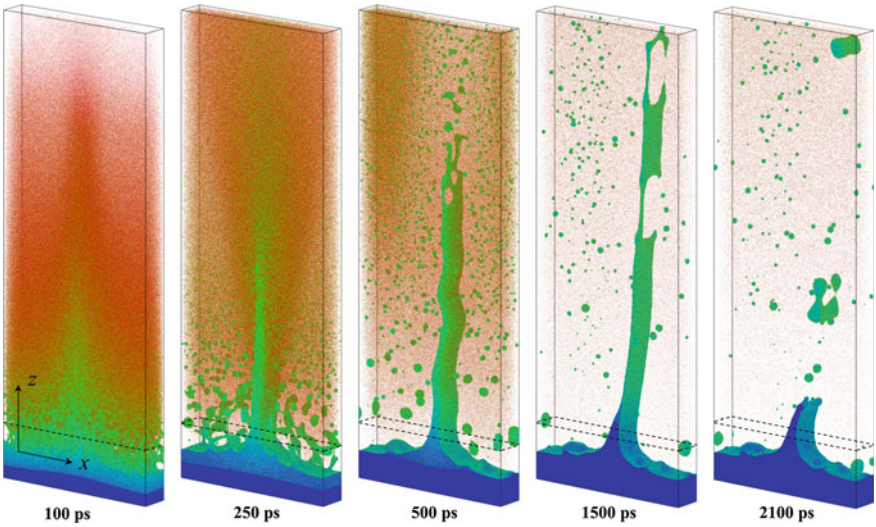

Fig. 5.13 A sequence of atomistic snapshots generated in a TTM-MD simulation of single pulse ablative LIPSS formation on a Cr surface. The snapshots show a part of the system with z coordinate ranging from −80 to 600 nm with respect to the location of the original surface of the target marked by the dashed rectangles. The atoms in the snapshots are colored by their potential energy, with color scale ranging from −3.8 eV (blue) to −1.4 eV (red). With this coloring scheme, dark-blue regions correspond to the solid phase, light-blue and green represent liquid phase and free surfaces, and red atoms belong to the vapor phase. The images are adapted from [163]

strated to yield important insights into the mechanisms and kinetics of complex, highly nonequilibrium processes involved in the laser-materials interactions. The examples provided in Sect. 5.4 illustrate the ability of large-scale MD simulations to reveal the critical information on the kinetics of laser-induced melting and resolidification, generation of crystal defects (vacancies, interstitials, dislocations, and twin boundaries), as well as the rapid material ejection and redistribution leading to the formation of LIPSS.

The remaining challenges include the incorporation of the detailed material-specific information on the electronic structure into the theoretical treatment of the transient optical and transport properties under conditions of strong electronic excitation, design of a reliable description of the metastable states, nonequilibrium phase transformations, and generation of crystal defects in the continuum-level models, as well as the extension of atomistic modeling to complex multi-component materials and multi-phase targets. Even more importantly, the development of integrated computational tools synergistically combining and enhancing the capabilities of different models is clearly needed in the field of modeling of laser-materials interactions. The factors that hamper the emergence of integrated models include the complexity of the task of combining dissimilar physical concepts and computational approaches, as well as the natural tendency of the research groups to focus on the areas of their expertise. Close and long-term interdisciplinary collaborations are

highly desired for making a disruptive progress in the theoretical and computational description of laser-materials interactions. The establishment of such collaborations, however, is often incompatible with current models of research funding, especially when international collaborations are involved. An additional challenge is presented by the computational complexity of models operating on different time and length scales and incorporating advanced mathematical algorithms. Optimization of computational codes for heterogeneous architectures of modern supercomputers is a task that requires continuous involvement of experts in the high-performance computing in the development of advanced multiscale models for laser-materials interactions.

Acknowledgements M.V.S., M.H., and L.V.Z. acknowledge financial support provided by the National Science Foundation (NSF) through Grants CMMI-1436775, CMMI-1562929, and DMR-1610936. S.A.L., Y.L., T.J.-Y.D., V.P.Z., and N.M.B. acknowledge financial support of the European Regional Development Fund and the state budget of the Czech Republic (project BIATRI: Grant No. CZ.02.1.01/0.0/0.0/15_003/0000445 and NPU I Project No. LO1602. Computational support enabling large-scale atomistic modeling was provided by the Oak Ridge Leadership Computing Facility (INCITE project MAT130) and NSF through the Extreme Science and Engineering Discovery Environment (project TG-DMR110090).

References

1. E.S. Massaro, A.H. Hill, E.M. Grumstrup, ACS Photon. **3**, 501 (2016)
2. A.M. Lindenberg, S.L. Johnson, D.A. Reis, Annu. Rev. Mater. Res. **47**, 425 (2017)
3. A. Barty, S. Boutet, M.J. Bogan, S. Hau-Riege, S. Marchesini, K. Sokolowski-Tinten, N. Stojanovic, R. Tobey, H. Ehrke, A. Cavalleri, S. Düsterer, M. Frank, S. Bajt, B.W. Woods, M.M. Seibert, J. Hajdu, R. Treusch, H.N. Chapman, Nat. Photon. **2**, 415 (2008)
4. M.V. Shugaev, C. Wu, O. Armbruster, A. Naghilou, N. Brouwer, D.S. Ivanov, T.J.-Y. Derrien, N.M. Bulgakova, W. Kautek, B. Rethfeld, L.V. Zhigilei, MRS Bull. **41**, 960 (2016)
5. C. Wu, E.T. Karim, A.N. Volkov, L.V. Zhigilei, in *Lasers in Materials Science*, ed. by M. Castillejo, P.M. Ossi, L.V. Zhigilei (Springer International Publishing, Switzerland, 2014), pp. 67–100
6. N.M. Bulgakova, V.P. Zhukov, in *Lasers in Materials Science*, ed. by M. Castillejo, P.M. Ossi, L.V. Zhigilei (Springer International Publishing, Switzerland, 2014), pp. 101–124
7. L.V. Zhigilei, Z. Lin, D.S. Ivanov, E. Leveugle, W.H. Duff, D. Thomas, C. Sevilla, S.J. Guy, in *Laser-Surface Interactions for New Materials Production: Tailoring Structure and Properties*, ed. by A. Miotello, P.M. Ossi (Springer, New York, 2010), pp. 43–79
8. N.M. Bulgakova, R. Stoian, A. Rosenfeld, I.V. Hertel, in *Laser-Surface Interactions for New Materials Production: Tailoring Structure and Properties*, ed. by A. Miotello, P.M. Ossi (Springer, New York, 2010), pp. 81–97
9. P. Drude, Ann. Phys. **306**, 566 (1900)
10. M.A. Ordal, R.J. Bell, R.W. Alexander, L.L. Long, M.R. Querry, Appl. Opt. **24**, 4493 (1985)
11. M.S. Dresselhaus, MIT Solid State Physics Course (2001)
12. K. Sokolowski-Tinten, D. von der Linde, Phys. Rev. B **61**, 2643 (2000)
13. F. Wooten, *Optical Properties of Solids* (Academic Press, New-York, 1972)
14. Y. Ren, J.K. Chen, Y. Zhang, J. Huang, Appl. Phys. Lett. **98**, 191105 (2011)
15. S.I. Ashitkov, P.S. Komarov, V.V. Zhakhovsky, Y.V. Petrov, V.A. Khokhlov, A.A. Yurkevich, D.K. Ilnitsky, N.A. Inogamov, M.B. Agranat, J. Phys.: Conf. Ser. **774**, 012097 (2016)
16. J. Zuo, A. Erbe, Phys. Chem. Chem. Phys. **12**, 11467 (2010)
17. A.D. Rakić, A.B. Djurišić, J.M. Elazar, M.L. Majewski, Appl. Opt. **37**, 5271 (1998)

18. H.S. Sehmi, W. Langbein, E.A. Muljarov, Phys. Rev. B **95**, 115444 (2017)
19. S.E. Kirkwood, Y.Y. Tsui, R. Fedosejevs, A.V. Brantov, V.Y. Bychenkov, Phys. Rev. B **79**, 144120 (2009)
20. Y.T. Lee, R.M. More, Phys. Fluids **27**, 1273 (1984)
21. D.V. Knyazev, P.R. Levashov, Phys. Plasmas **21**, 073302 (2014)
22. A.V. Brantov, V.Y. Bychenkov, W. Rozmus, J. Exp. Theor. Phys. **106**, 983 (2008)
23. H. Brysk, P.M. Campbell, P. Hammerling, Plasma Phys. **17**, 473 (1975)
24. Z. Lin, L.V. Zhigilei, V. Celli, Phys. Rev. B **77**, 075133 (2008)
25. M.B. Agranat, N.E. Andreev, S.I. Ashitkov, M.E. Veĭsman, P.R. Levashov, A.V. Ovchinnikov, D.S. Sitnikov, V.E. Fortov, K.V. Khishchenko, JETP Lett. **85**, 271 (2007)
26. E.I. Nefyodov, S.M. Smolskiy, *Understanding of Electrodynamics, Radio Wave Propagation and Antennas* (Scientific Research Publishing, Inc., 2013)
27. S.A. Furman, A.V. Tikhonravov, *Basics of Optics of Multilayer Systems* (Editions Frontières, Gif-Sur-Yvette, France, 1992)
28. O.A. Bulgakova, N.M. Bulgakova, V.P. Zhukov, Appl. Phys. A **101**, 53 (2010)
29. H. Raether, *Surface Plasmons on Smooth and Rough Surfaces and on Gratings* (Springer, Berlin, 1986)
30. E.D. Palik, *Handbook of Optical Constants of Solids* (Academic Press, San Diego, 1998)
31. C.-D. Wen, I. Mudawar, Int. J. Heat Mass Transf. **49**, 4279 (2006)
32. H.E. Bennett, J.O. Porteus, J. Opt. Soc. Am. **51**, 123 (1961)
33. J. Hohlfeld, U. Conrad, J.G. Muller, S.S. Wellerrshoff, E. Matthias, in *Nonlinear Optics in Metals*, ed. by K.H. Bennemann (Clarendon Press, Oxford, 1998), pp. 219–267
34. A.Y. Vorobyev, C. Guo, J. Appl. Phys. **110**, 043102 (2011)
35. S.I. Anisimov, B.L. Kapeliovich, T.L. Perel'man, Sov. Phys.—JETP **39**, 375 (1974)
36. S.A. Lizunov, R. Fang, A.Y. Vorobyev, V.P. Zhukov, N.M. Bulgakova, Ch. Guo, to be published (2018)
37. S.S. Wellershoff, J. Hohlfeld, J. Güdde, E. Matthias, Appl. Phys. A **69**, S99 (1999)
38. E. Bévillon, J.P. Colombier, V. Recoules, R. Stoian, Appl. Surf. Sci. **336**, 79 (2015)
39. O. Matsuda, O.B. Wright, D.H. Hurley, V. Gusev, K. Shimizu, Phys. Rev. B **77**, 224110 (2008)
40. Y. Levy, T.J.-Y. Derrien, N.M. Bulgakova, E.L. Gurevich, T. Mocek, Appl. Surf. Sci. **374**, 157 (2016)
41. N.A. Inogamov, Y.V. Petrov, J. Exp. Theor. Phys. **110**, 446 (2010)
42. J. Winter, S. Rapp, M. Schmidt, H.P. Huber, Appl. Surf. Sci. **417**, 2 (2017)
43. M.V. Shugaev, N.M. Bulgakova, Appl. Phys. A **101**, 103 (2010)
44. B. Rethfeld, A. Kaiser, M. Vicanek, G. Simon, Phys. Rev. B **65**, 214303 (2002)
45. J.E. Sipe, J.F. Young, J.S. Preston, H.M. Van Driel, Phys. Rev. B **27**, 1141 (1983)
46. J. Bonse, J. Krüger, S. Höhm, A. Rosenfeld, J. Laser Appl. **24**, 042006 (2012)
47. I. Gnilitskyi, T.J.-Y. Derrien, Y. Levy, N.M. Bulgakova, T. Mocek, L. Orazi, Sci. Rep. **7**, 8485 (2017)
48. Z. Chen, B. Holst, S.E. Kirkwood, V. Sametoglu, M. Reid, Y.Y. Tsui, V. Recoules, A. Ng, Phys. Rev. Lett. **110**, 135001 (2013)
49. B. Öktem, I. Pavlov, S. Ilday, H. Kalaycıoğlu, A. Rybak, S. Yavaş, M. Erdoğan, F.Ö. Ilday, Nat. Photon. **7**, 897 (2013)
50. A. Ruiz de la Cruz, R. Lahoz, J. Siegel, G.F. de la Fuente, J. Solis, Opt. Lett. **39**, 2491 (2014)
51. Y. Levy, N.M. Bulgakova, T. Mocek, Proc. SPIE **10228**, 102280T (2017)
52. P.P. Pronko, S.K. Dutta, D. Du, R.K. Singh, J. Appl. Phys. **78**, 6233 (1995)
53. N.M. Bulgakova, V.P. Zhukov, I. Mirza, Y.P. Meshcheryakov, J. Tomáštík, V. Michálek, O. Haderka, L. Fekete, A.M. Rubenchik, M.P. Fedoruk, T. Mocek, Proc. SPIE **9735**, 97350N (2016)
54. I. Mirza, N.M. Bulgakova, J. Tomáštík, V. Michálek, O. Haderka, L. Fekete, T. Mocek, Sci. Rep. **6**, 39133 (2016)
55. J.R. Peñano, P. Sprangle, B. Hafizi, W. Manheimer, A. Zigler, Phys. Rev. E **72**, 036412 (2005)
56. H.M. Van Driel, Phys. Rev. B **35**, 8166 (1987)
57. B.E. Sernelius, Phys. Rev. B **40**, 12438 (1989)

58. P. Saeta, J.K. Wang, Y. Siegal, N. Bloembergen, E. Mazur, Phys. Rev. Lett. **67**, 1023 (1991)
59. K. Sokolowski-Tinten, J. Bialkowski, D. Von Der Linde, Phys. Rev. B **51**, 14186 (1995)
60. A. Rousse, C. Rischel, S. Fourmaux, I. Uschmann, S. Sebban, G. Grillon, P. Balcou, E. Förster, J.P. Geindre, P. Audebert, J.C. Gauthier, D. Hulin, Nature **410**, 65 (2001)
61. H. Hu, H. Ding, F. Liu, Sci. Rep. **5**, 8212 (2015)
62. M. Beye, F. Sorgenfrei, W.F. Schlotter, W. Wurth, A. Fohlisch, Proc. Natl. Acad. Sci. **107**, 16772 (2010)
63. S. Sastry, C. Austen, Angell. Nat. Mater. **2**, 739 (2003)
64. V.V. Vasisht, S. Saw, S. Sastry, Nat. Phys. **7**, 549 (2011)
65. P. Stampfli, K.H. Bennemann, Phys. Rev. B **46**, 10686 (1992)
66. P. Silvestrelli, A. Alavi, M. Parrinello, D. Frenkel, Phys. Rev. Lett. **77**, 3149 (1996)
67. A. Gambirasio, M. Bernasconi, L. Colombo, Phys. Rev. B **61**, 8233 (2000)
68. H.O. Jeschke, M.E. Garcia, M. Lenzner, J. Bonse, J. Krüger, W. Kautek, Appl. Surf. Sci. **197–198**, 839 (2002)
69. E.S. Zijlstra, A. Kalitsov, T. Zier, M.E. Garcia, Phys. Rev. X **3**, 011005 (2013)
70. T. Zier, E.S. Zijlstra, A. Kalitsov, I. Theodonis, M.E. Garcia, Struct. Dyn. **2**, 054101 (2015)
71. C.V. Shank, R. Yen, C. Hirlimann, Phys. Rev. Lett. **50**, 454 (1983)
72. M. Combescot, J. Bok, J. Lumin. **30**, 1 (1985)
73. N.M. Bulgakova, I.M. Burakov, Y.P. Meshcheryakov, R. Stoian, A. Rosenfield, I.V. Hertel, J. Laser Micro/Nanoeng. **2**, 76 (2007)
74. R. Gunnella, G. Zgrablic, E. Giangrisostomi, F. D'Amico, E. Principi, C. Masciovecchio, A. Di Cicco, F. Parmigiani, Phys. Rev. B **94**, 155427 (2016)
75. E.N. Glezer, Y. Siegal, L. Huang, E. Mazur, Phys. Rev. B **51**, 6959 (1995)
76. T.J.-Y. Derrien, N.M. Bulgakova, Proc. SPIE **10228**, 102280E (2017)
77. T. Sjodin, H. Petek, H.-L. Dai, Phys. Rev. Lett. **81**, 5664 (1998)
78. M. Harb, R. Ernstorfer, T. Dartigalongue, C.T. Hebeisen, R.E. Jordan, R.J.D. Miller, J. Phys. Chem. B **110**, 25308 (2006)
79. C. Wu, L.V. Zhigilei, Appl. Phys. A **114**, 11 (2014)
80. R.F. Wood, G.E. Giles, Phys. Rev. B **23**, 2923 (1981)
81. K.N. Vonatsos, D.I. Pantelis, Appl. Phys. A **80**, 885 (2005)
82. I. Chowdhury, X. Xu, Numer. Heat Transf. Part A Appl. **219** (2003)
83. C. Wu, M.S. Christensen, J.M. Savolainen, P. Balling, L.V. Zhigilei, Phys. Rev. B **91**, 035413 (2015)
84. C. Wu, L.V. Zhigilei, J. Phys. Chem. C **120**, 4438 (2016)
85. M.V. Shugaev, C.Y. Shih, E.T. Karim, C. Wu, L.V. Zhigilei, Appl. Surf. Sci. **417**, 54 (2017)
86. X. Sedao, M.V. Shugaev, C. Wu, T. Douillard, C. Esnouf, C. Maurice, S. Reynaud, F. Pigeon, F. Garrelie, L.V. Zhigilei, J.-P. Colombier, ACS Nano **10**, 6995 (2016)
87. V. Gupta, H. Song, J. Im, MRS Proc. **397**, 465 (1995)
88. K.A. Jackson, Interface Sci. **10**, 159 (2002)
89. S.-N. Luo, T. Ahrens, T. Çağın, A. Strachan, W. Goddard, D. Swift, Phys. Rev. B **68**, 134206 (2003)
90. D.S. Ivanov, L.V. Zhigilei, Phys. Rev. Lett. **91**, 105701 (2003)
91. Z. Lin, L.V. Zhigilei, Phys. Rev. B **73**, 184113 (2006)
92. Z. Lin, E. Leveugle, E.M. Bringa, L.V. Zhigilei, J. Phys. Chem. C **114**, 5686 (2010)
93. D.S. Ivanov, Z. Lin, B. Rethfeld, G.M. O'Connor, T.J. Glynn, L.V. Zhigilei, J. Appl. Phys. **107**, 013519 (2010)
94. P.L. Liu, R. Yen, N. Bloembergen, R.T. Hodgson, Appl. Phys. Lett. **34**, 864 (1979)
95. Y. Fuentes-Edfuf, M. Garcia-Lechuga, D. Puerto, C. Florian, A. Garcia-Leis, S. Sanchez-Cortes, J. Solis, J. Siegel, Appl. Phys. Lett. **110**, 211602 (2017)
96. A. La Magna, V. Privitera, G. Fortunato, M. Cuscunà, B.G. Svensson, E. Monakhov, K. Kuitunen, J. Slotte, F. Tuomisto, Phys. Rev. B **75**, 235201 (2007)
97. T. Sinno, R.A. Brown, W. von Ammon, E. Dornberger, J. Electrochem. Soc. **145**, 302 (1998)
98. R.A. Brown, D. Maroudas, T. Sinno, J. Cryst. Growth **137**, 12 (1994)

99. E. Dornberger, T. Sinno, J. Esfandyari, J. Vanhellemont, R.A. Brown, W. von Ammon, Proc. Electrochem. Soc. **98**, 170 (1998)
100. L.V. Zhigilei, B.J. Garrison, J. Appl. Phys. **88**, 1281 (2000)
101. E. Leveugle, D.S. Ivanov, L.V. Zhigilei, Appl. Phys. A **79**, 1643 (2004)
102. G. Paltauf, P.E. Dyer, Chem. Rev. **103**, 487 (2003)
103. L.V. Zhigilei, Z. Lin, D.S. Ivanov, J. Phys. Chem. C **113**, 11892 (2009)
104. J.M. Savolainen, M.S. Christensen, P. Balling, Phys. Rev. B **84**, 193410 (2011)
105. A.A. Ionin, S.I. Kudryashov, A.E. Ligachev, S.V. Makarov, L.V. Seleznev, D.V. Sinitsyn, JETP Lett. **94**, 266 (2011)
106. S.I. Ashitkov, N.A. Inogamov, V.V. Zhakhovskii, Y.N. Emirov, M.B. Agranat, I.I. Oleinik, S.I. Anisimov, V.E. Fortov, JETP Lett. **95**, 176 (2012)
107. S.V. Starikov, V.V. Pisarev, J. Appl. Phys. **117**, 135901 (2015)
108. A. Lomonosov, A.P. Mayer, P. Hess, in *Modern Acoustical Techniques for the Measurement of Mechanical Properties*, ed. by M. Levy, H. Bass, R. Stern (Academic Press, San Diego, California, 2001), pp. 65–134
109. P. Hess, Phys. Today **55**, 42 (2002)
110. V.V. Kozhushko, A.M. Lomonosov, P. Hess, Phys. Rev. Lett. **98**, 195505 (2007)
111. C. Krischer, D. Lichtman, Phys. Lett. A **44**, 99 (1973)
112. B. Lindner, U. Seydel, Anal. Chem. **57**, 895 (1985)
113. V.V. Golovlev, S.L. Allman, W.R. Garrett, C.H. Chen, Appl. Phys. Lett. **71**, 852 (1997)
114. A.V. Zinovev, I.V. Veryovkin, J.F. Moore, M.J. Pellin, Anal. Chem. **79**, 8232 (2007)
115. A.M. Dow, A.R. Wittrig, H.I. Kenttämaa, Eur. J. Mass Spectrom. **18**, 77 (2012)
116. A.J. Manzo, H. Helvajian, Proc. SPIE **8969**, 896908 (2014)
117. M.V. Shugaev, A.J. Manzo, C. Wu, V.Y. Zaitsev, H. Helvajian, L.V. Zhigilei, Phys. Rev. B **91**, 235450 (2015)
118. C. Wu, V.Y. Zaitsev, L.V. Zhigilei, J. Phys. Chem. C **117**, 9252 (2013)
119. B.S. Yilbas, J. Phys. D Appl. Phys. **35**, 1210 (2002)
120. D.Y. Tzou, E.J. Pfautsch, J. Eng. Math. **61**, 231 (2008)
121. Y.-M. Lee, T.-W. Tsai, J. Phys. D Appl. Phys. **41**, 045308 (2008)
122. Y.P. Meshcheryakov, M.V. Shugaev, T. Mattle, T. Lippert, N.M. Bulgakova, Appl. Phys. A **113**, 521 (2013)
123. Y.P. Meshcheryakov, N.M. Bulgakova, Appl. Phys. A **82**, 363 (2006)
124. E. Vanagas, J. Kawai, D. Tuzhilin, I. Kudryashov, A. Mizuyama, K.G. Nakamura, K. Kondo, S. Koshihara, M. Takesada, K. Matsuda, S. Juodkazis, V. Jarutis, S. Matsuo, H. Misawa, J. Microlithogr. Microfabr. Microsyst. **3**, 358 (2004)
125. J. Bohandy, B.F. Kim, F.J. Adrian, J. Appl. Phys. **60**, 1538 (1986)
126. I. Zergioti, S. Mailis, N.A. Vainos, C. Fotakis, S. Chen, C.P. Grigoropoulos, Appl. Surf. Sci. **127–129**, 601 (1998)
127. M. Domke, S. Rapp, M. Schmidt, H.P. Huber, Appl. Phys. A **109**, 409 (2012)
128. D. Munoz-Martin, C.F. Brasz, Y. Chen, M. Morales, C.B. Arnold, C. Molpeceres, Appl. Surf. Sci. **366**, 389 (2016)
129. G. Heise, M. Englmaier, C. Hellwig, T. Kuznicki, S. Sarrach, H.P. Huber, Appl. Phys. A **102**, 173 (2011)
130. G. Heise, M. Domke, J. Konrad, S. Sarrach, J. Sotrop, H.P. Huber, J. Phys. D Appl. Phys. **45**, 315303 (2012)
131. D.S. Ivanov, B. Rethfeld, G.M. O'Connor, T.J. Glynn, A.N. Volkov, L.V. Zhigilei, Appl. Phys. A **92**, 791 (2008)
132. N.A. Inogamov, V.V. Zhakhovsky, K.P. Migdal, Appl. Phys. A **122**, 432 (2016)
133. J. Sotrop, A. Kersch, M. Domke, G. Heise, H.P. Huber, Appl. Phys. A **113**, 397 (2013)
134. A. Miotello, R. Kelly, Appl. Phys. Lett. **67**, 3535 (1995)
135. N.M. Bulgakova, A.V. Bulgakov, Appl. Phys. A **73**, 199 (2001)
136. B.J. Garrison, T.E. Itina, L.V. Zhigilei, Phys. Rev. E **68**, 041501 (2003)
137. J. Dowden (ed.), *The Theory of Laser Materials Processing. Heat and Mass Transfer in Modern Technology* (Springer, Dordrecht, 2009)

138. D. Bäuerle, *Laser Processing and Chemistry* (Springer, Berlin, 2000)
139. C. Earl, J.R. Castrejón-Pita, P.A. Hilton, W. O'Neill, J. Manuf. Process. **21**, 214 (2016)
140. W.R. Harp, J.R. Dilwith, J.F. Tu, J. Mater. Process. Technol. **198**, 22 (2008)
141. V. Semak, A. Matsunawa, J. Phys. D Appl. Phys. **30**, 2541 (1997)
142. B.S. Yilbas, S.B. Mansoor, J. Phys. D Appl. Phys. **39**, 3863 (2006)
143. S.P. Harimkar, A.N. Samant, N.B. Dahotre, J. Appl. Phys. **101**, 054911 (2007)
144. Y.L. Yao, H. Chen, W. Zhang, Int. J. Adv. Manuf. Technol. **26**, 598 (2005)
145. V.S. Ajaev, D.A. Willis, Cit. Phys. Fluids **15**, 3144 (2003)
146. A.N. Volkov, L.V. Zhigilei, Int. J. Heat Mass Transf. **112**, 300 (2017)
147. C.-Y. Shih, C. Wu, H. Wu, M.V Shugaev, in *Pulsed Laser Ablation: Advances and Applications in Nanoparticles and Nanostructuring Thin Films*, ed. by I.N. Mihailescu, A.P. Caricato (Pan Stanford, 2018), pp. 421–466
148. Z. Lin, R.A. Johnson, L.V. Zhigilei, Phys. Rev. B **77**, 214108 (2008)
149. C. Wu, D.A. Thomas, Z. Lin, L.V. Zhigilei, Appl. Phys. A **104**, 781 (2011)
150. X. Sedao, C. Maurice, F. Garrelie, J.-P. Colombier, S. Reynaud, R. Quey, F. Pigeon, Appl. Phys. Lett. **104**, 171605 (2014)
151. D.S. Ivanov, L.V. Zhigilei, Phys. Rev. B **68**, 064114 (2003)
152. P.P. Pronko, S.K. Dutta, J. Squier, J.V. Rudd, D. Du, G. Mourou, Opt. Commun. **114**, 106 (1995)
153. J. Koch, F. Korte, T. Bauer, C. Fallnich, A. Ostendorf, B.N. Chichkov, Appl. Phys. A **81**, 325 (2005)
154. A.I. Kuznetsov, J. Koch, B.N. Chichkov, Appl. Phys. A **94**, 221 (2009)
155. U. Zywietz, A.B. Evlyukhin, C. Reinhardt, B.N. Chichkov, Nat. Commun. **5**, 3402 (2014)
156. J. Jersch, F. Demming, J. Hildenhagen, K. Dickmann, Opt. Laser Technol. **29**, 433 (1998)
157. A. Chimmalgi, T.Y. Choi, C.P. Grigoropoulos, K. Komvopoulos, Appl. Phys. Lett. **82**, 1146 (2003)
158. D. Hwang, S.G. Ryu, N. Misra, H. Jeon, C.P. Grigoropoulos, Appl. Phys. A **96**, 289 (2009)
159. C. Huber, A. Trügler, U. Hohenester, Y. Prior, W. Kautek, Phys. Chem. Chem. Phys. **16**, 2289 (2014)
160. Y. Nakata, T. Okada, M. Maeda, Jpn. J. Appl. Phys. **42**, L1452 (2003)
161. D.S. Ivanov, V.P. Lipp, A. Blumenstein, F. Kleinwort, V.P. Veiko, E. Yakovlev, V. Roddatis, M.E. Garcia, B. Rethfeld, J. Ihlemann, P. Simon, Phys. Rev. Appl. **4**, 064006 (2015)
162. X.W. Wang, A.A. Kuchmizhak, X. Li, S. Juodkazis, O.B. Vitrik, Y.N. Kulchin, V.V. Zhakhovsky, P.A. Danilov, A.A. Ionin, S.I. Kudryashov, A.A. Rudenko, N.A. Inogamov, Phys. Rev. Appl. **8**, 044016 (2017)
163. M.V. Shugaev, I. Gnilitskyi, N.M. Bulgakova, L.V. Zhigilei, Phys. Rev. B, **96**, 205429 (2017)
164. J. Bonse, A. Rosenfeld, J. Krüger, J. Appl. Phys. **106**, 104910 (2009)
165. D.L. Andrews, G.D. Scholes, G.P. Wiederrecht, *Comprehensive Nanoscience and Nanotechnology*, 4th ed. (Elsevier, Academic Press, 2011)
166. R. Buividas, M. Mikutis, S. Juodkazis, Prog. Quantum Electron. **38**, 119 (2014)
167. B. Dusser, Z. Sagan, H. Soder, N. Faure, J.P. Colombier, M. Jourlin, E. Audouard, Opt. Express **18**, 2913 (2010)
168. J. Reif, O. Varlamova, F. Costache, Appl. Phys. A **92**, 1019 (2008)
169. M. Gedvilas, J. Mikšys, G. Račiukaitis, RSC Adv. **5**, 75075 (2015)
170. E.L. Gurevich, Appl. Surf. Sci. **374**, 56 (2016)
171. I. Gnilitskyi, V. Gruzdev, N.M. Bulgakova, T. Mocek, L. Orazi, Appl. Phys. Lett. **109**, 143101 (2016)
172. E.L. Gurevich, Y. Levy, S.V. Gurevich, N.M. Bulgakova, Phys. Rev. B **95**, 54305 (2017)